J. Fluid Mech. (2008), *vol.* 605, *pp.* 293–327.
doi:10.1017/S0022112008001535 Printed in the United Kingdom

Viscoplastic fluid displacements in horizontal narrow eccentric annuli: stratification and travelling wave solutions

M. CARRASCO-TEJA[1], I. A. FRIGAARD[1,2]†, B. R. SEYMOUR[1] AND S. STOREY[2]

[1]Department of Mathematics, University of British Columbia, 1984 Mathematics Road, Vancouver, BC, V6T 1Z2, Canada

[2]Department of Mechanical Engineering, University of British Columbia, 2054-6250 Applied Science Lane, BC, V6T 1Z4, Canada

(Received 30 September 2007 and in revised form 11 March 2008)

We consider laminar displacement flows in narrow eccentric annuli, oriented horizontally, between two fluids of Herschel–Bulkley type, (i.e. including Newtonian, power-law and Bingham models). This situation is modelled via a Hele-Shaw approach. Whereas slumping and stratification would be expected in the absence of any imposed flow rate, for a displacement flow we show that there are often steady-state travelling wave solutions in this displacement. These may exist even at large eccentricities and for large density differences between the fluids. When heavy fluids displace light fluids, annular eccentricity opposes buoyancy and steady states are more prevalent than when light fluids displace heavy fluids. For large ratios of buoyancy forces to viscous forces we derive a lubrication-style displacement model. This simplification allows us to find necessary and sufficient conditions under which a displacement can be steady, which can be expressed conveniently in terms of a consistency ratio. It is interesting that buoyancy does not appear in the critical conditions for a horizontal well. Instead a competition between fluid rheologies and eccentricity is the determining factor. Buoyancy acts only to determine the axial length of the steady-state profile.

1. Introduction

The aim of this paper is to derive conditions under which displacement flows of Herschel–Bulkley fluids along a narrow eccentric annulus may either advance as a steady travelling wave or stratify gravitationally. The annulus is oriented horizontally, perpendicular to the direction of gravity, see figure 1. The motivation for the study comes from the industrial process of primary cementing, used to complete oil wells prior to production. Since the early 1990s there has been a great increase in the numbers of oil wells constructed horizontally, primarily to increase productivity by aligning the well with the reservoir. The increase in length of horizontal wells was made possible by advances in directional drilling technology. The early 1990s saw a continual increasing of the horizontal reach of wells up to around 10 km, see e.g. the detailed description in Payne, Wilton & Ramos. (1995). The 10 km barrier was broken in a number of wells drilled at Wytch Farm, UK, in around 2000. The

† Author to whom correspondence should be addressed: frigaard@mech.ubc.ca

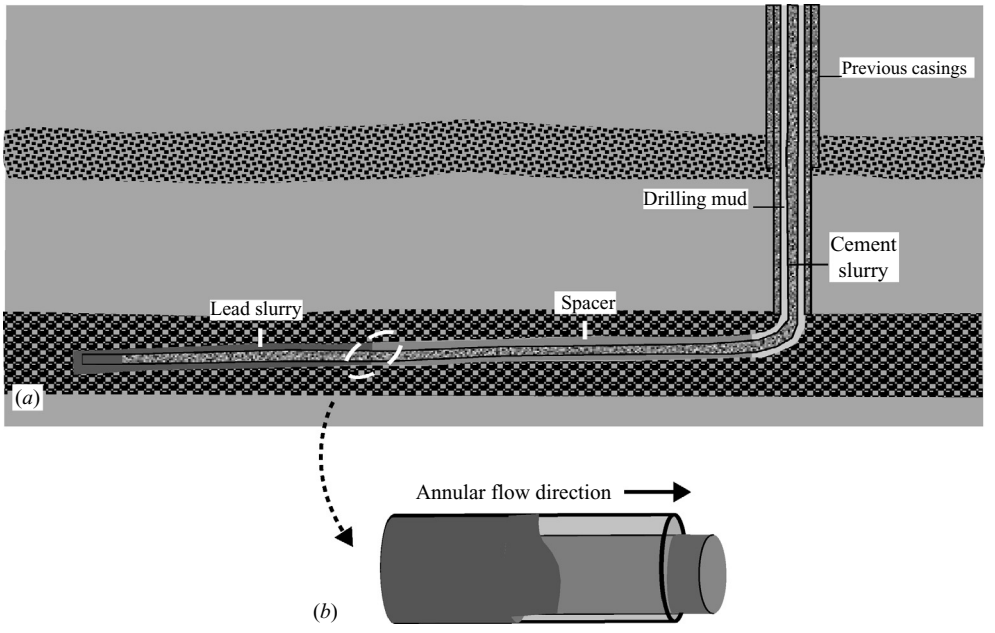

FIGURE 1. Schematic of the primary cementing displacement in a horizontal well: process schematic.

limits of 'extreme' extended reach wells are now being pushed into the 15 – 20 km range, but such wells are unusual and do not necessarily bring productivity benefits proportional to their technical challenges. In the present day it is routinely feasible to construct wells with horizontal extensions in the 7 – 10 km range.

Many of the other well construction technologies have lagged behind in this surge in construction of long horizontal wells, cementing being one of these. Although many of the potential problems of cementing horizontal wells were identified some time ago, e.g. Sabins (1990), the industrial response has been largely through technological advances, rather than by developing understanding of physical fundamentals that may affect the process. In this paper we adopt the latter approach and consider the fluid dynamics of displacement during primary cementing of horizontal wells. The primary cementing process involves the displacement of one non-Newtonian fluid by another, pumped axially along the annulus at a constant imposed flow rate. The flows that we consider are laminar and the annuli considered have annular gaps that are narrow with respect to both circumferential and axial length scales. Thus, a Hele-Shaw modelling approach is appropriate and we adopt a two-dimensional model derived by Bittleston, Ferguson & Frigaard (2002), outlined in §2. Those unfamiliar with this process may consult Nelson (1990) for background information.

In cementing near-vertical wells it is advantageous to maintain a positive density and viscosity difference between successive fluid stages pumped. This helps to offset the destabilizing effects of the annulus eccentricity and has long been advocated in the industrial literature, although without a firm scientific basis. In the sequence of papers Pelipenko & Frigaard (2004*a–c*) a more rational understanding of the displacement dynamics in near-vertical annuli was developed using a Hele-Shaw model. It was shown that under certain process conditions it is possible to obtain steady travelling wave displacement front solutions that are stable. Conditions were derived that predict the occurrence of these steady solutions and, in certain simple situations,

analytic expressions are found for their shapes. Here this predictive understanding is extended to displacements in horizontal annuli. For brevity the reader is referred to the introductory sections of the above papers for a review of related work and industrial motivation.

In primary cementing, see Nelson (1990), successive casings or liners are fitted within one another, thus decreasing the size of the new hole that can be drilled. For this reason, longer extended reach wells tend to be of smaller diameter and also tend to be cemented increasingly in laminar flow regimes. This latter is due to smaller annular gap sizes and to the increased risk of high frictional pressures fracturing the surrounding formation at high flow rates. Thus, for modelling the fluid mechanics of the displacement process, long horizontal wells are the process situation that offers the widest range of validity of the Hele-Shaw approach.

In the absence of a density difference between fluids, displacements in horizontal annuli are the same as in vertical annuli. However, drilling fluids are typically 100–600 $\mathrm{kg/m^{-3}}$ less dense than cement slurries, and a chemically compatible spacer fluid designed to have intermediate density and rheological properties typically separates these two fluids. Therefore density differences are inevitable in the cementing of horizontal wells. A number of questions arise that are both of fluid mechanic interest and of practical industrial relevance.

(*a*) Which dimensionless groups govern whether or not the flow will become stratified? In the worst case, stratification could allow the displacing fluid to completely by-pass the displaced fluid, rendering the displacement ineffective.

(*b*) With a density difference, is it possible to have steady travelling wave displacement fronts? What characteristics of these fronts can be predicted: shape, stability, etc?

(*c*) What are the effects of an increased flow rate on a horizontal displacement?

Finally, we might suspect that the typical shapes of displacement fronts are different in horizontal annuli than in vertical annuli. In vertical annuli, eccentricity tends to promote dispersive spreading on the wide side of the annulus, where the fluid velocities are larger. This effect is countered by positive viscosity and density differences, eventually resulting in steady travelling wave displacement fronts. In eccentric horizontal annuli the heavy steel casing is likely to lie to the lower side of the borehole. It appears that two types of mechanically stable separated flow may develop, see figure 2. First, suppose that there is a positive density difference strong enough to force the heavier displacing fluid azimuthally around to the narrow side of the annulus. In this case a heavy finger of displacing fluid advances along the bottom of the annulus ahead of the mean flow and we have the configuration of figure 2(*a*). Second, suppose there is no density difference or that the displacing fluid is lighter than the displaced fluid (figure 2*b*). In this case we may expect a 'classical' form of separated flow to develop in which the displacing fluid advances ahead along the wide upper side of the annulus. These two basic types of flows can also be found experimentally. As an illustration, figure 3 shows an example result from recent laboratory experiments, with slumping along the bottom.

The aim of our paper is to answer some of the above questions and to develop a qualitative and quantitative understanding of these displacement flows. Our main tool for this is a simplified version of the Hele-Shaw displacement model from Bittleston *et al.* (2002), restricted to a well section of constant inclination, eccentricity and radii, which we outline in §2. We then explore some typical results of numerical simulations conducted with the two-dimensional model (in §3). The two-dimensional simulations are relatively time consuming as it is necessary to resolve potential regions

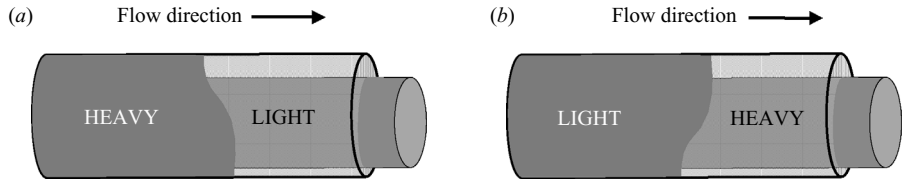

FIGURE 2. Schematic of mechanically stable separated flow configurations in a horizontal displacement: (*a*) heavy fluid displacing; (*b*) light fluid displacing.

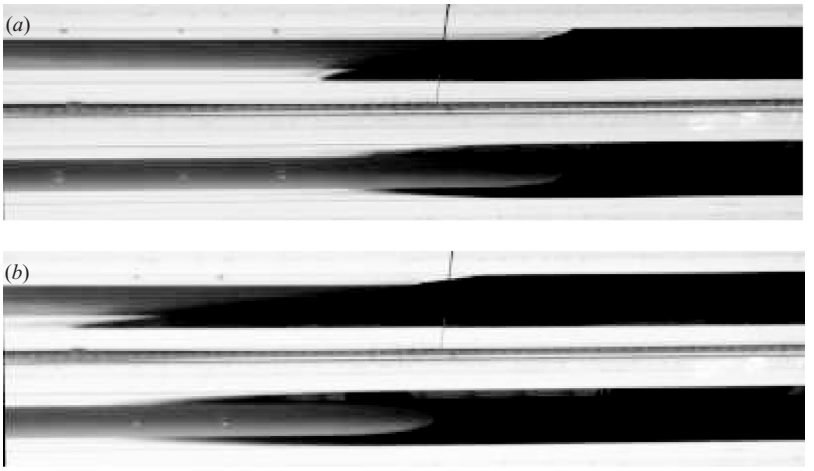

FIGURE 3. An example of slumping along the bottom of a horizontal concentric annulus: fluid 1 ($\hat{\rho}_1 = 1398$ kg/m^{-3}, $\hat{\kappa}_1 = 6.24$ Pa s, $n_1 = 1$), coloured black with dye, displaces fluid 2 ($\hat{\rho}_2 = 1363$ kg/m^{-3}, $\hat{\kappa}_2 = 0.76$ Pa s, $n_2 = 1$), moving from right to left at mean speed 1.6 mm s^{-1}. Each subfigure shows a side view and a view from above the annulus (centrebody is grey); image (*b*) is taken after image (*a*), after 116.5 ml of fluid 1 has been pumped.

of unyielded fluid in the annulus, which is achieved using an iterative approach; see Pelipenko & Frigaard (2004*b*). Another difficulty with the two-dimensional model is that these flows are governed by 11 dimensionless parameters, describing the rheology, density/buoyancy and well geometry, which makes broad parametric study of the flow regimes near-impossible. A last problem is that many of the displacement flows extend along the annulus axially a significant distance, which of course increases the size of numerical domain (and hence computational cost) needed for two-dimensional simulation.

The above factors motivate our development in §4 of a lubrication/thin-film model. Elongation of the interface is found when $|\tilde{b}| \gg 1$, where $\tilde{b}$ denotes the ratio of buoyancy and viscous forces. In this limit, an evolution equation for the propagation of the volumetric interface location may be derived, which is a one-dimensional quasi-linear advection–diffusion equation. This equation may be solved relatively quickly but may also be analysed. We show that it is possible to predict the conditions under which a steady travelling wave solution can be found for the lubrication limit. Necessary and sufficient conditions for the existence of steady-state travelling wave solutions are given and we survey the (parametrically simpler) set of steady interface shapes and stability maps. The paper closes with a summary of results and discussion of consequences in §5.

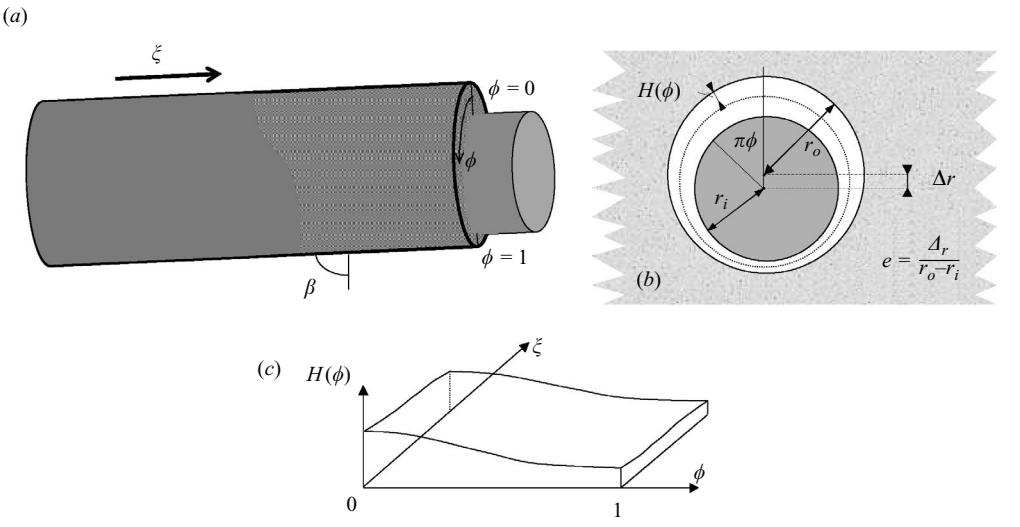

FIGURE 4. Geometry of the narrow eccentric annulus, mapped to the Hele-Shaw cell geometry: (*a*) near-horizontal annulus; (*b*) annular gap geometry and eccentricity; (*c*) unwrapped half-annular and half-gap Hele-Shaw geometry.

2. Hele-Shaw modelling of cementing displacements

We consider the model developed by Bittleston *et al.* (2002), simplified so that the annulus is locally uniform in the axial direction, i.e. over a length scale that is long in comparison to the azimuthal scale, and only two fluids will be considered. The model and all parameters used in this paper are dimensionless, with dimensional parameters only referred to to highlight the physical meaning of certain parameters. In this case, any dimensional quantity will be distinguished by a caret symbol, e.g. $\hat{\rho}_1$. A summary of the scaling used is given just before §2.1 below. Further details may be found in Bittleston *et al.* (2002) or Pelipenko & Frigaard (2004*a*).

The axis is at a fixed angle of inclination, $\beta \approx \pi/2$, to the vertical, see figure 4. As in the model used in Bittleston *et al.* (2002) and Pelipenko & Frigaard (2004*a*) averaging across the narrow annular gap eliminates radial variations, thus effectively unwrapping the annulus into a Hele-Shaw cell, see figure 4. The dimensionless spatial coordinates are $(\phi, \xi) \in (0, 1) \times (0, Z)$. ϕ is the azimuthal coordinate with $\phi = 0$ denoting the wide side of the annulus and $\phi = 1$ the narrow (lower) side. The flow is assumed symmetric about $\phi = 0$, and thus only half the annulus is considered. This assumption implies that the narrow side of the annulus is always lying on the low side of the well. The ξ coordinate measures axial depth along the annulus in the direction of the mean flow, see figure 4. Z denotes the length of the section of well to be cemented. $Z \gg 1$, since the length scale used for scaling the equations is one half the mean circumference, typically ≈ 0.5 m, whereas lengths of cemented sections are in the $100 - 1000$ m range. The half-gap width H varies only with ϕ and is defined by

$$H(\phi) = 1 + e \cos \pi\phi, \tag{2.1}$$

which is a narrow gap approximation. Here $e \in [0, 1)$ is the annulus eccentricity (see figure 2); $e = 0$ corresponds to a concentric annulus, $e = 1$ implies contact between the casing and outer wall, on the narrow side of the annulus.

The annulus is initially full of fluid 2, which is displaced by fluid 1. Although the fluids are miscible, the time scale for molecular diffusion to have significant effects is typically much longer than other process time scales. Thus the interface is essentially advected, and we consider two standard ways to model its motion. First, we consider a fluid concentration formulation in which $\overline{c}$ denotes the concentration of fluid 1, assumed not to vary across the annular gap width. The gap-averaged concentration equation (minus any diffusion) is simply:

$$\frac{\partial}{\partial t}\left[H\overline{c}\right] + \frac{\partial}{\partial \phi}\left[H\overline{v}\ \overline{c}\right] + \frac{\partial}{\partial \xi}\left[H\overline{w}\ \overline{c}\right] = 0, \tag{2.2}$$

where the averaged velocity components in the (ϕ, ξ)-directions are $(\overline{v}, \overline{w})$. A second approach, that is more convenient for our later analysis, is to track the interface via a gap-averaged kinematic equation; this approach is described in §2.1.

The fluids are incompressible so that $(\overline{v}, \overline{w})$ are written in terms of a stream function Ψ where

$$\frac{\partial \Psi}{\partial \phi} = H\overline{w}, \qquad \frac{\partial \Psi}{\partial \xi} = -H\overline{v}. \tag{2.3}$$

Boundary conditions for (2.2) and (2.3) are symmetry of concentration at $\phi = 0,\ 1$, and specification of any inflowing fluid concentrations at the ends, $\xi = 0,\ Z$, i.e. $\overline{c} = 0$ or $\overline{c} = 1$, accordingly.

The underlying fluids are modelled as Herschel-Bulkley fluids: $m = 1/n$ is the inverse power law index, τ_Y is the yield stress and κ is the consistency. For a Newtonian fluid $m = 1$ and $\tau_Y = 0$. We assume that the fluids are shear-thinning throughout ($m \geqslant 1$), since this is usual with oil field fluids. In the concentration approach, these fluid properties will depend on $\overline{c}$, as will the fluid density, ρ.

The stream function is found from the elliptic field equation

$$\nabla\cdot[\boldsymbol{S} + \boldsymbol{f}] = 0, \tag{2.4}$$

that is derived by cross-differentiating the relevant Darcy law to eliminate the pressure. This is the standard procedure in a Hele-Shaw flow law if one wishes to work with the stream function and not the pressure. For the stream function equation (2.4), boundary conditions are

$$\Psi(0, \xi, t) = 0, \qquad \Psi(1, \xi, t) = 1, \tag{2.5}$$

$$\frac{\partial \Psi}{\partial \xi}(\phi, Z, t) = 0, \qquad \frac{\partial \Psi}{\partial \xi}(\phi, 0, t) = 0. \tag{2.6}$$

The relevant closure law is derived in Bittleston *et al.* (2002), from which

$$\boldsymbol{S} = \left[\frac{\chi(|\nabla\Psi|) + \tau_Y/H}{|\nabla\Psi|}\right]\nabla\Psi \iff |S| > \frac{\tau_Y}{H}, \tag{2.7}$$

$$|\nabla\Psi| = 0 \iff |S| \leqslant \frac{\tau_Y}{H}, \tag{2.8}$$

where the function $\chi = \chi(|\nabla\Psi|; H, \tau_Y, \kappa, m)$ is defined implicitly from the relation:

$$|\nabla\Psi| = \begin{cases} 0 & (\chi \leqslant 0), \\ \dfrac{H^{m+2}}{\kappa^m(m+2)}\dfrac{\chi^{m+1}}{(\chi + \tau_Y/H)^2}\left[\chi + \dfrac{(m+2)\tau_Y}{(m+1)H}\right] & (\chi > 0). \end{cases} \tag{2.9}$$

Underlying (2.7)–(2.9) is a model of the flow of a Herschel-Bulkley fluid along a plane channel in the direction of the modified pressure gradient; see Appendix A

for an outline of the model. If $|\boldsymbol{S}| \leqslant \tau_Y/H$ then $|\nabla\Psi| = 0$, and there is no fluid flow. Physically the modified pressure gradient $|\boldsymbol{S}|$ is not strong enough to overcome the yield stress in that section of the annulus. At such points $\boldsymbol{S}$ is bounded but is indeterminate. At those points where $|\nabla\Psi| > 0$ the fluid is flowing. All buoyancy terms have been collected together in (2.4) in the term $\boldsymbol{f}$:

$$\boldsymbol{f} = \left(\frac{\rho(\bar{c})\cos\beta}{St^*}, \frac{\rho(\bar{c})\sin\beta\sin\pi\phi}{St^*} \right), \tag{2.10}$$

where St^* is the global Stokes number for the flow, defined by

$$St^* = \frac{\hat{\mu}^*\hat{w}^*}{\hat{\rho}^*\hat{g}(\hat{d}^*)^2}.$$

To recover dimensional quantities, note that the axial and azimuthal velocities have been scaled with the mean flow velocity, $\hat{w}^*$, lengths with the half-circumference $\pi\hat{r}_a^*$ (here $\hat{r}_a^*$ is the mean radius). A rate-of-strain scale is obtained by dividing $\hat{w}^*$ by the half-gap width, $\hat{d}^* = (\hat{r}_o - \hat{r}_i)/2$, and this used with the constitutive laws to derive a viscosity scale, $\hat{\mu}^*$, defined as the maximal effective viscosity at the mean shear rate. The pressure gradient balances with the leading-order shear-stress scale, as always in a Hele-Shaw flow. Finally, $\hat{\rho}^*$ is the density scale (defined as the larger of the two unmixed fluid densities), and $\hat{g}$ the gravitational acceleration.

2.1. *Interface tracking*

The formulation with (2.2) requires that the interface is interpreted as a contour of the concentration field, e.g. $\bar{c}(\phi, \xi, t) = 0.5$, and also that closure laws be specified for the mixture fluid properties, i.e. as functions of $\bar{c}$. The domain is divided into two fluid domains: Ω_1 for the displacing (lower) fluid 1, and Ω_2 for the displaced (upper) fluid 2, in each of which (2.4) is replaced by

$$\nabla\cdot\boldsymbol{S}_1 = 0, \qquad (\phi, \xi) \in \Omega_1, \tag{2.11}$$

$$\nabla\cdot\boldsymbol{S}_2 = 0, \qquad (\phi, \xi) \in \Omega_2, \tag{2.12}$$

with $\boldsymbol{S}_1$ and $\boldsymbol{S}_2$ defined as in (2.7)–(2.8), with properties ρ_1, $\tau_{1,Y}$, κ_1, m_1 in fluid 1 and ρ_2, $\tau_{2,Y}$, κ_2, m_2 in fluid 2. The interface is denoted by $\phi = \phi_i(\xi, t)$, and satisfies the kinematic condition:

$$\frac{\partial\phi_i}{\partial t} + \bar{w}\frac{\partial\phi_i}{\partial\xi} = \bar{v}. \tag{2.13}$$

The leading-order continuity conditions at the interface are that the stream function Ψ and the pressure p are continuous across the interface. Assuming sufficient regularity of the interface, the former condition enssures that the normal velocity, the derivative of Ψ along the interface, is well-defined at the interface. Pressure continuity is expressed in terms of defining the jump in $\boldsymbol{S}_k$ across the interface:

$$\left[\left(S_{k,\xi}\frac{\partial\phi_i}{\partial\xi} - S_{k,\phi} \right) + \left(\frac{\rho_k\sin\beta\sin\pi\phi}{St^*}\frac{\partial\phi_i}{\partial\xi} - \frac{\rho_k\cos\beta}{St^*} \right) \right]_1^2 = 0. \tag{2.14}$$

Equation (2.14) also defines the jump in the normal derivative of Ψ across the interface.

3. Horizontal displacement flows

We now start to build our intuition of the types of displacement phenomena that we are likely to find in laminar horizontal well cementing flows. Treated in full generality,

we see that displacements are governed by the following 11 dimensionless parameters: rheology $\tau_{k,Y}$, κ_k, n_k, $k = 1, 2$; density/buoyancy ρ_k, $k = 1, 2$, St^*; well geometry, e and β. For the concentration–advection formulation, all 11 parameters are needed since intermediate values of $\bar{c}$ are computed. In addition closure laws are needed for the rheology and density at intermediate concentrations. Although cumbersome in terms of the large parameter space, the concentration–advection formulation is the easiest to deal with computationally, and we present a number of results from this model below.

For analytical results the interface tracking formulation is more convenient. In this formulation, ρ_k, $k = 1, 2$, and St^* may be replaced by a buoyancy number $\tilde{b}$:

$$\tilde{b} = \frac{\rho_2 - \rho_1}{St^*}, \tag{3.1}$$

as this is the only combination in which these parameters appear in the jump conditions at the interface. For strictly horizontal wells $\beta = \pi/2$, and thus we are reduced to the six dimensionless rheological parameters, plus e and $\tilde{b}$.

Here we present a number of results computed using the concentration–advection formulation. The numerical method used is that described in detail in Pelipenko & Frigaard (2004*b*). At a given time step, assuming the concentrations and stream function are known, we differentiate the stream function to give the velocity field and advance the concentration one time step. For this we use the FCT scheme, see Zalesak (1979), on a staggered rectangular mesh. The concentrations are approximated at the cell centres and the stream function at the corners. Thus partial derivatives of the stream function along the edges give the required velocity components. Given concentrations at the new time step, the stream function is computed from (2.4), which is solved using the augmented Lagrangian approach with the Uzawa-like algorithm. Computations presented below have been solved with mesh spacings $\Delta\phi = 1/40$ and $\delta\xi = 1/20$.

As a test problem, we consider a concentric annulus displacement between two Newtonian fluids, for which there is a steady travelling wave solution:

$$\xi - t = -\frac{\tilde{b}\cos\pi\phi}{3\pi[\kappa_2 - \kappa_1]} + \text{constant},$$

see Pelipenko & Frigaard (2004*a*). Results of the computation for $\kappa_1 = 1$, $\kappa_2 = 0.25$, $\rho_1 = 1$, $\rho_2 = 0.9$, $St^* = 0.05$, ($\Longrightarrow \tilde{b} = -2$), are shown in figure 5. In this and subsequent plots, the ϕ-axis points vertically downwards, with the wide side at the top of each figure and the narrow side at the bottom, as would be the case in a horizontal well. The direction of flow is always from left to right, in the direction of increasing ξ.

Figure 5(*a*) shows the contour $\bar{c}(\phi, \xi, t) = 0.5$ plotted at successive time intervals $\Delta t = 0.5$. We start the simulation with the annulus full of fluid 2 for $\xi \geqslant 1$, and fluid 1 in $\xi < 1$. We see a quick evolution to a steadily advancing profile. Figure 5(*b*) plots the above analytical solution at the same time intervals. Figure 5(*c*) overlays the computed and analytical profiles in the latter part of the annulus. We see that the agreement is good, with similar shapes and a constant offset. If the same example is repeated with no density difference, a steady planar displacement front is found. The addition of the positive density difference evidently results in slumping of the heavy fluid towards the lower side of the well. It is interesting to note that with a significant buoyancy effect (i.e. $|\tilde{b}| = O(1)$) complete stratification does not occur in this case.

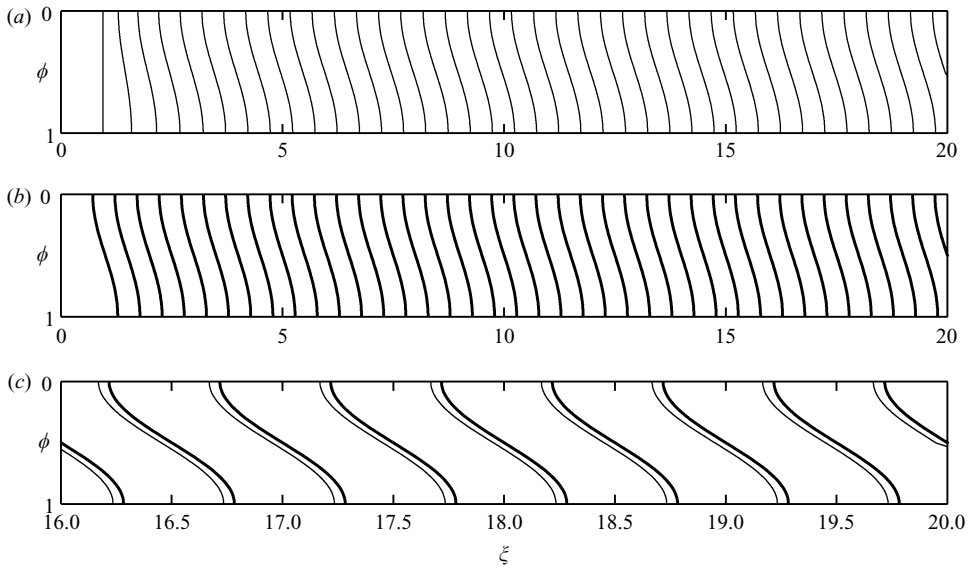

FIGURE 5. Test problem, comparing two-dimensional computations with the analytical solution from Pelipenko & Frigaard (2004*a*), with parameters: $e = 0$, $\beta = \pi/2$, $\tau_{Y,k} = 0$, $n_k = 1$, $\kappa_1 = 1$, $\kappa_2 = 0.25$, $\rho_1 = 1$, $\rho_2 = 0.9$, $St^* = 0.05$. (*a*) The contour $\bar{c}(\phi, \xi, t) = 0.5$ at time intervals $\Delta t = 0.5$. (*b*)The analytical interface position (steady-state solution from Pelipenko & Frigaard (2004*a*)), plotted at time intervals $\Delta t = 0.5$. (*c*) Comparison of numerical (thin) and analytical (thick) solutions.

In practice it is possible for the displacing fluid (fluid 1) to be either heavier or lighter than the displaced fluid. A heavier and more viscous fluid 1 might result when using a classical design for near-vertical wells, as positive density and viscosity gradients help a vertical displacement, see Pelipenko & Frigaard (2004*c*). Regardless of the wellbore inclination, at some point during a displacement there is always likely to be a positive density gradient between fluid stages, simply because the density of cement slurries is typically higher than that of drilling muds. For all positive density differences (heavy displacing light), we intuitively expect to see slumping of the displacing fluid to the bottom of the well, as in the test case above.

Although less common, there are also situations in which the displacing fluid may be lighter, and either more or less viscous. For example, if a wash is pumped ahead of the cement slurry it will generally be lighter and less viscous than the drilling mud. Other than this, various lightweight spacer fluids have been used in displacing and these may be lighter but more viscous than the drilling mud. In either case, the expected effect of the density difference is to promote stratification, with the light fluid moving ahead along the top of the annulus.

3.1. *Heavy displacing fluids,* $\tilde{b} < 0$

We first consider the more common case, where the displacing fluid is heavier than the displaced ($\tilde{b} < 0$). In figure 6 we present results of the same displacement as in figure 5, but with a mildly eccentric annulus, $e = 0.1$. The effect of eccentricity is to promote faster flow on the wide side of the annulus, $\phi = 0$, and in the absence of any density difference the interface is usually found to advance further along the wide side than the narrow side. Thus, we can see that there is a competition between the effects of eccentricity and buoyancy, promoting interfacial advances on the wide and

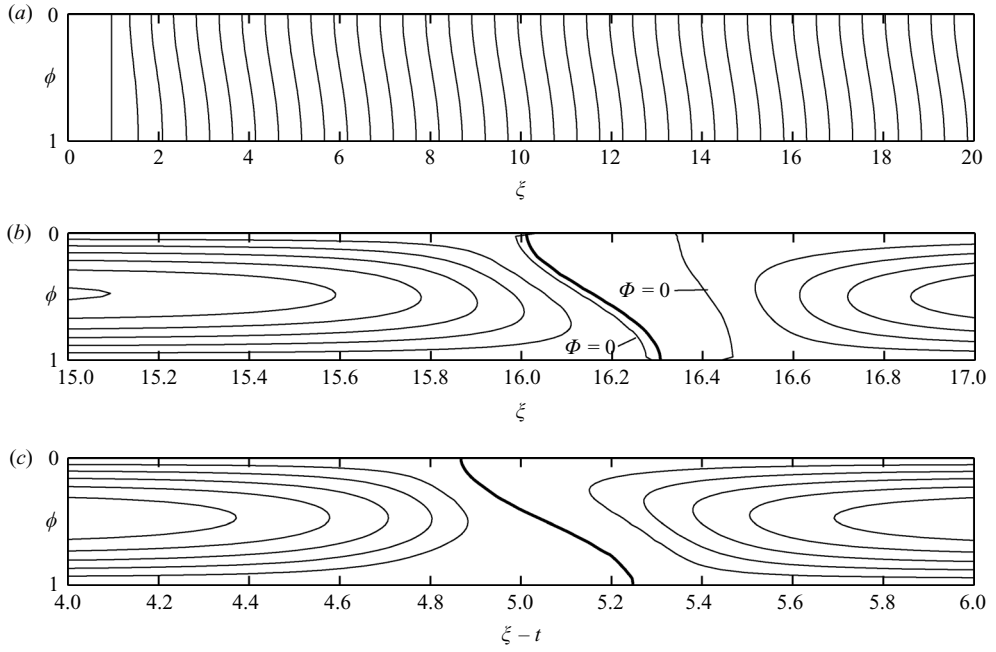

FIGURE 6. Newtonian displacement at $St^* = 0.05$ with positive buoyancy gradient in a mildly eccentric annulus. Parameters: $e = 0.1$, $\beta = \pi/2$, $\tau_{Y,k} = 0$, $n_k = 1$, $\kappa_1 = 1$, $\kappa_2 = 0.25$, $\rho_1 = 1$, $\rho_2 = 0.9$. (*a*) The contour $\bar{c}(\phi, \xi, t) = 0.5$ at time intervals $\Delta t = 0.5$. (*b*) The moving-frame stream function $\Phi(\phi, \xi, t)$ at $t = 15.5$, with the contour $\bar{c}(\phi, \xi, t) = 0.5$ (heavy line); contours are $\Phi = 0,\ 0.01,\ 0.02,\ 0.03,\ 0.04,\ 0.05,\ 0.06$. (*c*). The moving-frame stream function $\Phi(\phi, \xi - t, t)$ at $t = 40$, with the contour $\bar{c}(\phi, \xi - t, t) = 0.5$ (heavy line); contours are $\Phi = 0.01,\ 0.02,\ 0.03,\ 0.04,\ 0.05$.

narrow side respectively. Figure 6(*a*) plots the evolution of the (interface) contour, $\bar{c}(\phi, \xi, t) = 0.5$, at time intervals $\Delta t = 0.5$. The eccentricity–buoyancy competition is evident: the interface initially slumps then appears to recover slightly. The axial extent of the steady-state interface is ≈ 0.4, whereas for $e = 0$ it was ≈ 0.5, i.e. eccentricity has reduced the extent of slumping along the wellbore axis.

Figure 6(*b*) plots contours of the moving-frame stream function $\Phi(\phi, \xi, t)$:

$$\Phi(\phi, \xi, t) = \Psi(\phi, \xi, t) - \int_0^{\phi} H(\tilde{\phi})\, \mathrm{d}\tilde{\phi}, \tag{3.2}$$

at $t = 15.5$. The stream function $\Phi(\phi, \xi, t)$ simply subtracts the effects of a uniform mean axial velocity field from $\Psi(\phi, \xi, t)$, and is appropriate for identifying steady travelling wave solutions. Figure 6(*b*) shows an $O(1)$ recirculation zone within the $\Phi(\phi, \xi, t) = 0$ contour. The interface contour, $\bar{c}(\phi, \xi, t) = 0.5$ (heavy line), is overlaid on the figure and lies within this zone. This large recirculatory zone is responsible for the slightly transitory behaviour in figure 6(*a*). The two (near vertical) $\Phi = 0$ contours divide the domain into three regions. In the two end regions $\Phi(\phi, \xi, t) > 0$ and the circulation is clockwise. The displacing fluid moves from the wide to narrow side and the displaced fluid moves from the narrow to wide side. In the central cell we have $\Phi(\phi, \xi, t) < 0$ and the circulation is counter-clockwise, but relatively slow. This $O(1)$ central recirculation zone is not steady, but contracts slowly during the displacement, eventually becoming a single line between the wide and narrow sides. To

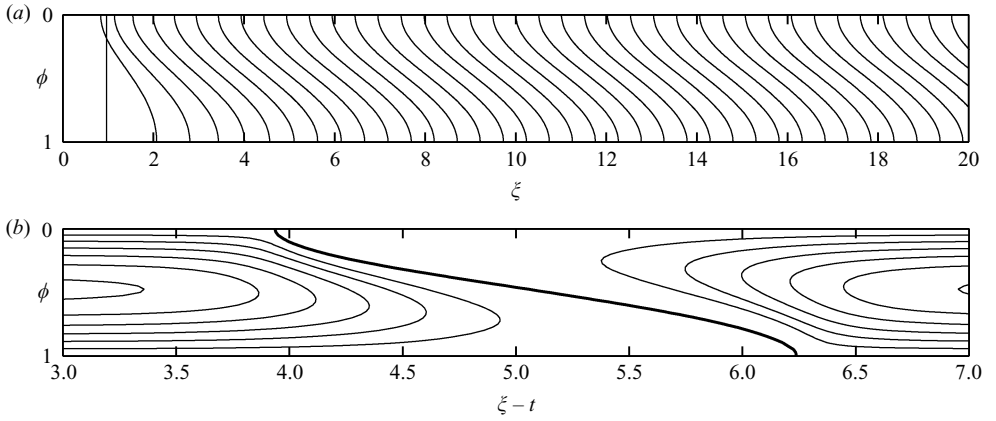

FIGURE 7. Newtonian displacement at $St^* = 0.01$ with positive buoyancy gradient in a mildly eccentric annulus. Parameters: $e = 0.1$, $\beta = \pi/2$, $\tau_{Y,k} = 0$, $n_k = 1$, $\kappa_1 = 1$, $\kappa_2 = 0.25$, $\rho_1 = 1$, $\rho_2 = 0.9$. (*a*) The contour $\bar{c}(\phi, \xi, t) = 0.5$ at time intervals $\Delta t = 0.5$. (*b*): The moving frame stream function $\Phi(\phi, \xi - t, t)$ at $t = 40$, with the contour $\bar{c}(\phi, \xi - t, t) = 0.5$ (heavy line); contours are $\Phi = 0.01,\ 0.02,\ 0.03,\ 0.04,\ 0.05,\ 0.06$.

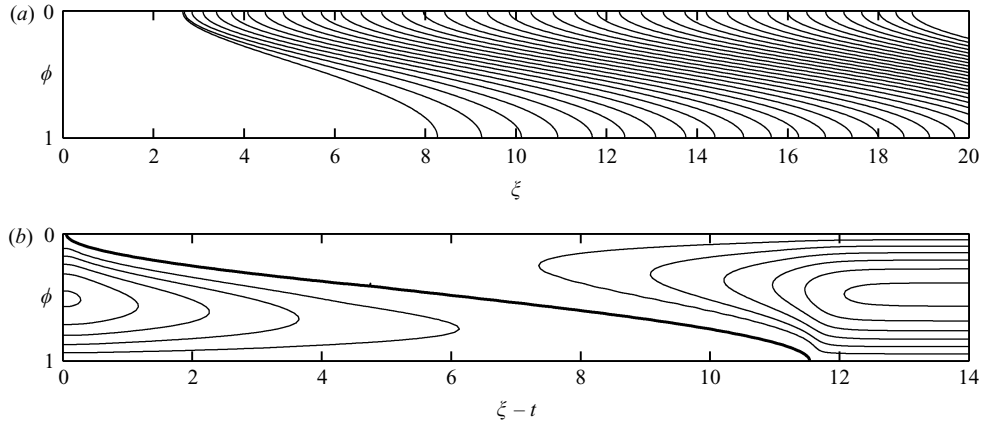

FIGURE 8. As figure 7 but with $St^* = 0.002$.

avoid computations with a very large mesh, long-time computations are carried out in a steadily moving frame of reference. Figure 6(*c*) shows the contours of Φ and the interface contour , $\bar{c} = 0.5$, in the moving frame at $t = 40$. In this frame of reference the streamlines and concentration are steady. We observe that buoyancy effects are dominant with the steady finger advanceing along the bottom of the annulus.

Two further Newtonian fluid computations are presented in figures 7 and 8, in which the Stokes number is decreased to $St^* = 0.01$ and $St^* = 0.002$ respectively. The parameters are otherwise the same as in figure 6. The decrease in St^* physically corresponds to a reduction in dimensional flow rate, which reduces viscous stresses. In the Hele-Shaw model only viscous and buoyant forces are present and balance each other. Thus, as expected, reducing St^* amplifies the relative effects of buoyancy and a slumping flow occurs. Figures 7(*a*) and 8(*b*) show the evolution of the interface contour $\bar{c} = 0.5$. Figures 7(*b*) and 8(*b*) show the streamlines $\Phi(\phi, \xi - t, t)$, computed in the moving frame of reference, after a time $t = 40$. What is perhaps surprising is

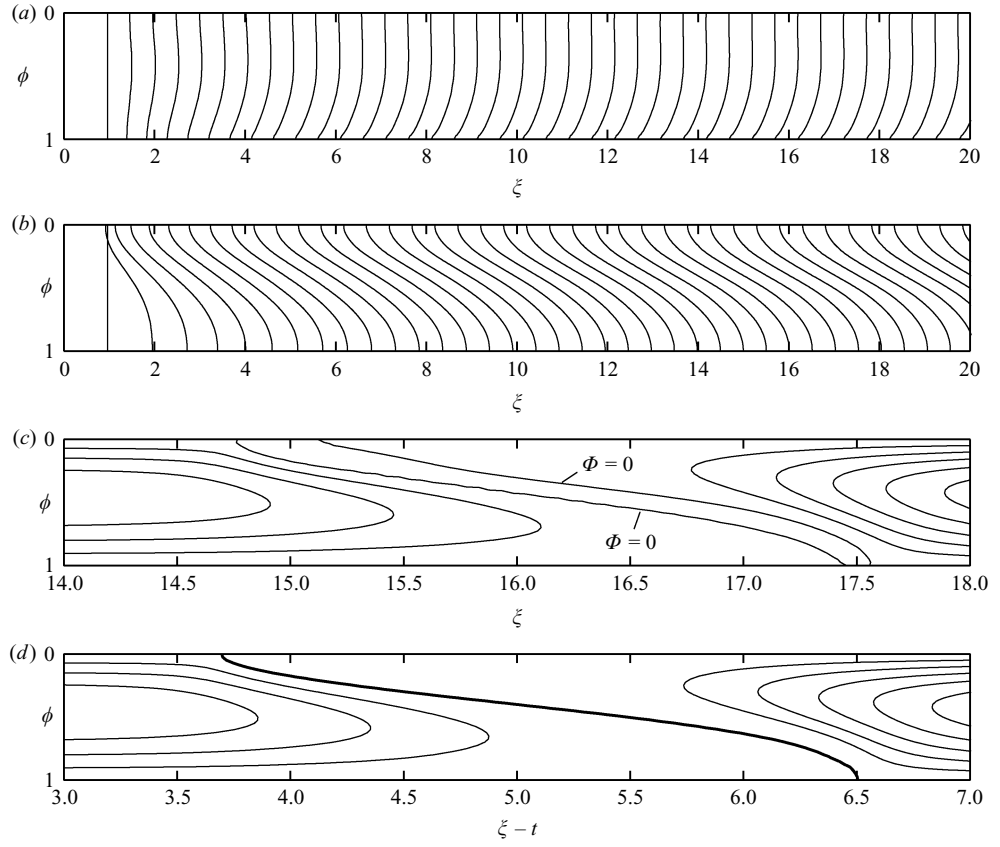

FIGURE 9. Non-Newtonian displacement with positive buoyancy gradient in an eccentric annulus. Parameters: $e = 0.2$, $\beta = \pi/2$, $\tau_{Y,1} = 0$, $\tau_{Y,2} = 1$, $n_k = 1$, $\kappa_1 = 1$, $\kappa_2 = 0.25$, $\rho_1 = 1$, $\rho_2 = 0.9$. (*a*) $St^* = 0.05$, contour $\bar{c}(\phi, \xi, t) = 0.5$ at time intervals $\Delta t = 0.5$. (*b*) $St^* = 0.01$, contour $\bar{c}(\phi, \xi, t) = 0.5$ at time intervals $\Delta t = 0.5$. (*c*) $St^* = 0.01$, the moving-frame stream function $\Phi(\phi, \xi, t)$ at $t = 15.5$; contours are $\Phi = 0,\ 0.03,\ 0.06,\ 0.09,\ 0.12,\ 0.15$. (*d*) $St^* = 0.01$, the moving-frame stream function $\Phi(\phi, \xi - t, t)$ at $t = 40$, with the contour $\bar{c}(\phi, \xi - t, t) = 0.5$ (heavy line); contours are $\Phi = 0.03,\ 0.06,\ 0.09,\ 0.12,\ 0.15$.

that even with this massively increased buoyancy effect, the flow settles to a steady state, i.e. complete stratification does not occur. However, the steady state does stretch along the annulus axis a greater distance as St^* is decreased. In the absence of an imposed flow rate, we would expect that the flow would stratify.

Two natural questions arise. First, if we keep increasing the relative effects of buoyancy, in an example such as that in figures 6–8, will we always have a steadystate travelling wave interface solution albeit extending further along the annulus, or is there a point at which the fluids stratify? We investigate this limit and the associated question in §4.

Secondly, we ask whether in all cases buoyancy will be dominant, or can the slumping motion be arrested via annular eccentricity and/or by rheological effects? The answer here is yes. In figure 9 we show a non-Newtonian displacement at eccentricity $e = 0.2$, with a yield stress in the displaced fluid, $\tau_{Y,2} = 1$ (all other parameters remaining as before). At $St^* = 0.05$, figure 9(*a*) shows the evolution of the interfacial contour $\bar{c} = 0.5$. With the added eccentricity and yield stress, flow

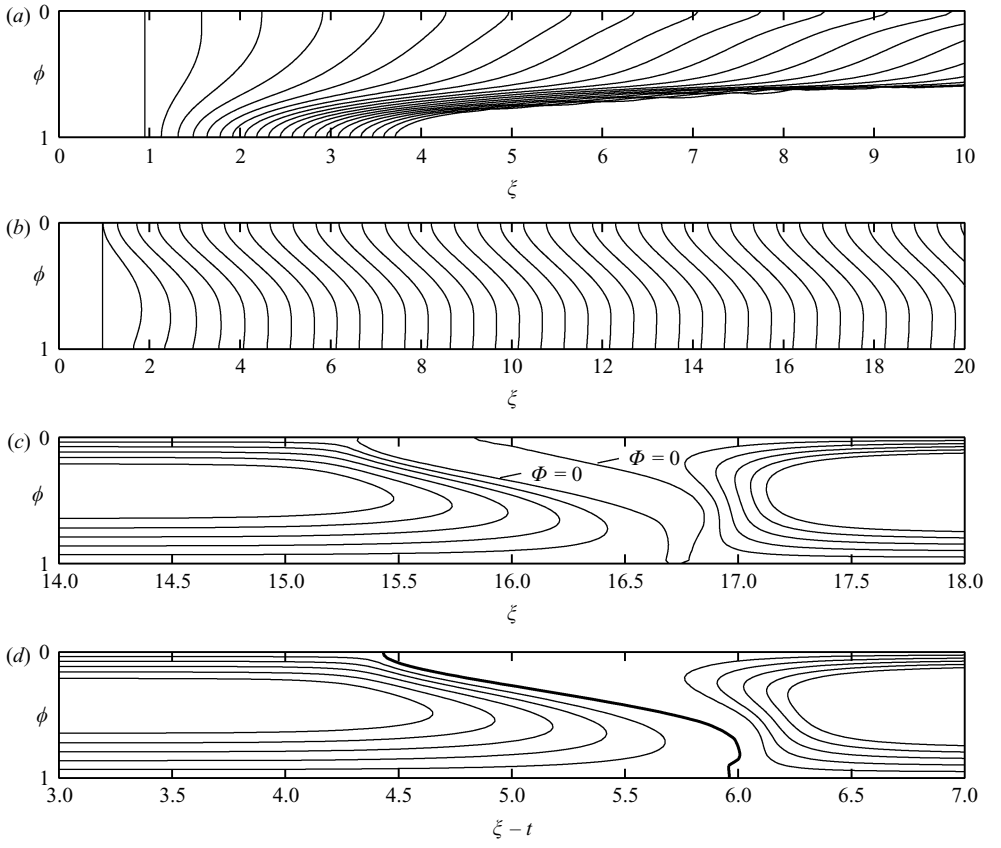

FIGURE 10. As figure 9 but with eccentricity, $e = 0.4$.

is retarded on the narrow side and we instead observe that the finger advances ahead on the upper wider side of the annulus. On reducing the Stokes number to $St^* = 0.01$, buoyancy again dominates. Figure 9(*b*) shows the evolution of the interfacial contour $\bar{c} = 0.5$. There is again slow transitory behaviour as eccentricity and buoyancy compete, characterized by a transitory recirculatory zone (see figure 9*c*), before eventually the steady-state profile is attained, see figure 9(*d*). Figure 10 shows results of the same simulation but at $e = 0.4$. The unsteady fingering at $St^* = 0.05$ is now obvious (figure 10*a*), but again decreasing St^* results in a steady travelling wave, figure 10(*b–d*).

3.2. *Light displacing fluids,* $\tilde{b} > 0$

Turning now to the situation where the displacing fluid is less dense, we first examine Newtonian displacements with a mildly eccentric annulus. The primary difference with the previous subsection is that now both buoyancy and eccentricity promote stratification along the top (wide) side of the annulus. Only rheological differences may be used to counter the tendency to finger along the wide side of the annulus. In the absence of any positive viscosity difference, we must expect that the interface will advance rapidly along the wide side, quickly becoming parallel with the annulus axis. An example of this is shown in figure 11, with parameters $\kappa_1 = 0.25$, $\kappa_2 = 1$, a 10% density difference, $e = 0.2$ and $St^* = 0.05$ (Newtonian fluids).

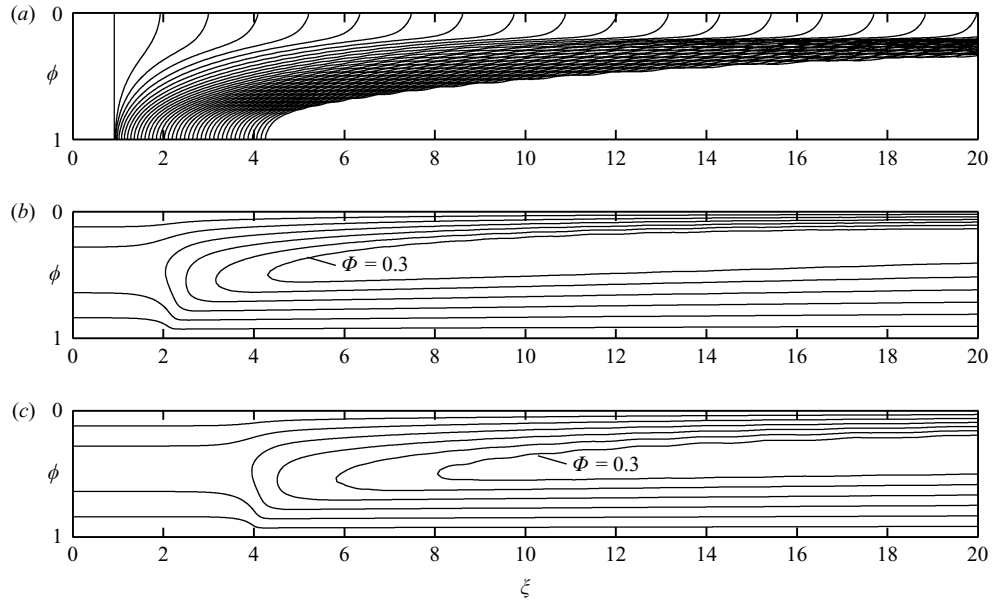

FIGURE 11. Newtonian displacement with negative buoyancy gradient in an eccentric annulus. Parameters: $St^* = 0.05$, $e = 0.2$, $\beta = \pi/2$, $\tau_{Y,k} = 0$, $n_k = 1$, $\kappa_1 = 0.25$, $\kappa_2 = 1$, $\rho_1 = 0.9$, $\rho_2 = 1$. (*a*) Contour $\bar{c}(\phi, \xi, t) = 0.5$ at time intervals $\Delta t = 0.5$. (*b*) The moving-frame stream function $\Phi(\phi, \xi, t)$ at $t = 10$; contours are $\Phi = 0.05,\ 0.1,\ 0.15,\ 0.2,\ 0.25,\ 0.3$. (*c*) As (*b*), but at $t = 20$.

With the viscosity difference of figure 11 reversed, the effect is very different, see figure 12. The initial displacement advances along the wide side of the annulus, but does not succeed in fully stratifying. Over intermediate time scales there again persists a zone of counter-clockwise circulation, figure 12(*b*), which acts to partly steepen the interface and then contracts to a steady-state profile, see figure 12(*c*). It appears that this positive viscosity gradient ($\kappa_1 = 1$, $\kappa_2 = 0.25$) is sufficient to displace in a steady state at $e = 0.2$.

With non-Newtonian fluids little is changed fundamentally: eccentricity and buoyancy are destabilizing but for certain rheological combinations it is possible to achieve a steady-state displacement. One example of this is shown in figure 13. The results are qualitatively similar to that of figure 12. An initial acceleration along the wide side is followed by a transitional motion of the interface via a slowly contracting weak counter-clockwise rotation and finally the profile converges to a steady state at longer times.

3.3. *Summary*

We have run a number of computations for both positive and negative buoyancy differences, from which several of conclusions may be drawn. First, the same solution types are found regardless of the sign of the buoyancy difference (steady front or unsteady finger), and the form of approach to the steady state is also identical. Where the density difference is positive (heavy fluids displace light fluids) buoyant slumping and eccentricity compete, whereas for negative density differences they act together. However, in both cases significant rheological differences between the fluids can determine whether or not the displacement is steady.

From the two-dimensional simulations that we have run, we are in a position to at least postulate what sufficient conditions for a steady-state should be. In a horizontal

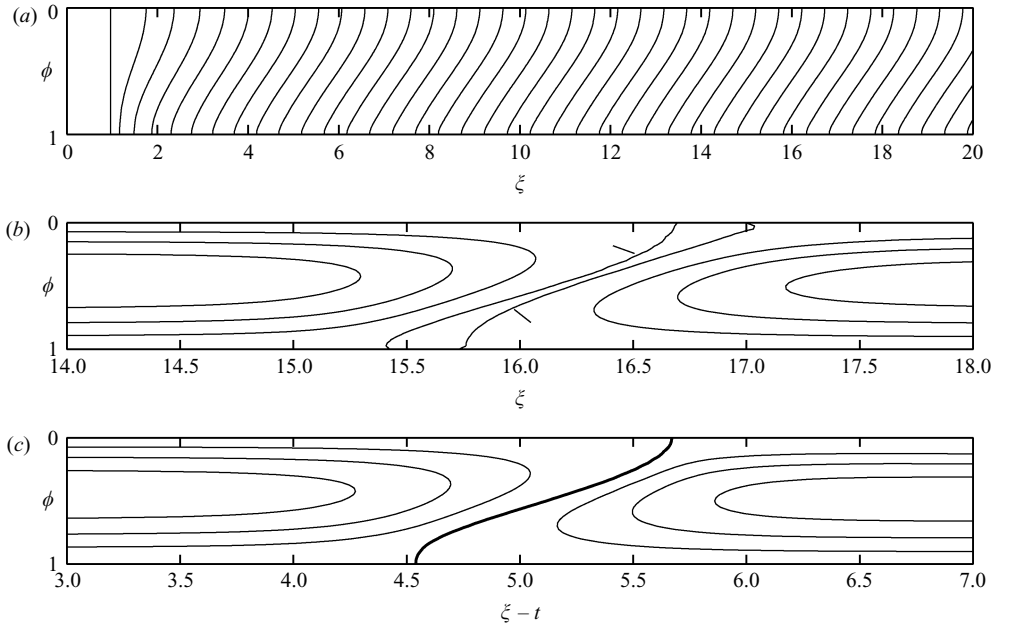

FIGURE 12. Newtonian displacement with negative buoyancy gradient in an eccentric annulus. Parameters: $St^* = 0.05$, $e = 0.2$, $\beta = \pi/2$, $\tau_{Y,k} = 0$, $n_k = 1$, $\kappa_1 = 1$, $\kappa_2 = 0.25$, $\rho_1 = 0.9$, $\rho_2 = 1$. (*a*) Contours $\bar{c}(\phi, \xi, t) = 0.5$ at time intervals $\Delta t = 0.5$. (*b*) The moving frame stream function $\Phi(\phi, \xi, t)$ at $t = 15.5$, contours $\Phi = 0,\ 0.03,\ 0.06,\ 0.09,\ 0.12,\ 0.15$. (*c*). The moving-frame stream function $\Phi(\phi, \xi - t, t)$ at $t = 40$, with the contour $\bar{c}(\phi, \xi - t, t) = 0.5$ (heavy line); contours are $\Phi = 0.03,\ 0.06,\ 0.09,\ 0.12,\ 0.15$.

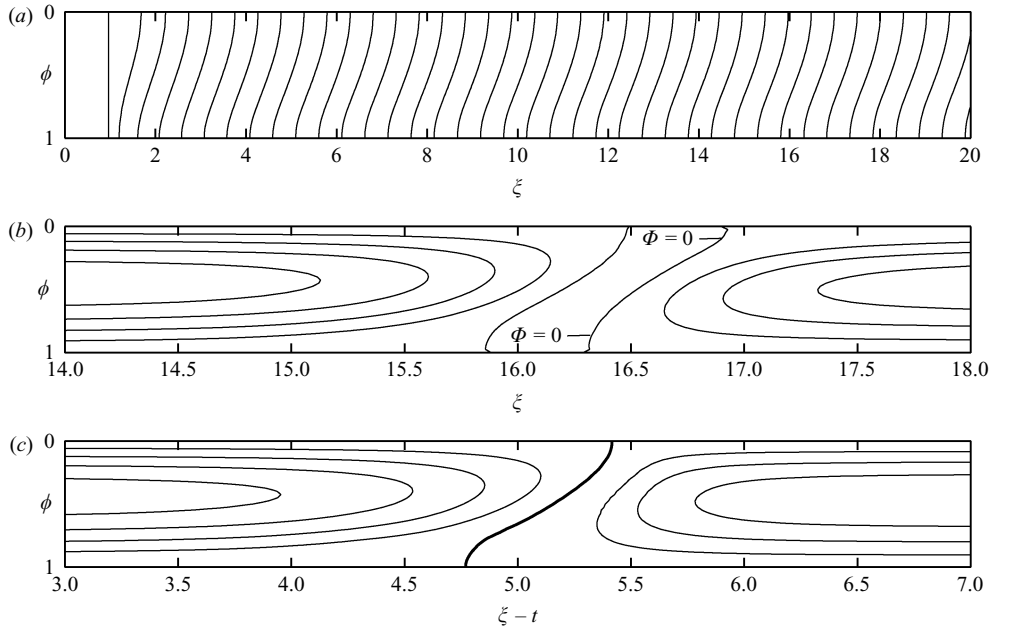

FIGURE 13. Non-Newtonian displacement with negative buoyancy gradient in an eccentric annulus. As figure 12 but with $\tau_{Y,1} = 1$, $\kappa_2 = 0.05$.

well displacement, under the Hele-Shaw assumptions of our model, buoyancy forces act only azimuthally. These contribute to the axial momentum balance only through the slope of the interface. As the interface elongates along the well the contribution of the azimuthal buoyancy forces is diminished. The only exception to this would be at the wide and narrow side of the annulus, where the interface may run perpendicular to the annulus axis. However, the buoyancy force acts azimuthally with magnitude proportional to $\sin \pi\phi$, and thus vanishes on the wide and narrow sides. Therefore, we might postulate that a sufficient condition for the two-dimensional simulation to have a steady-state displacement solution is that the corresponding iso-density displacement has a steady state displacement. However, results such as those in figure 10 contradict this statement.

Of key practical interest is to determine whether or not the displacement is steady. Our two-dimensional computations are not ideal for this purpose for a number of reasons. Some of these reasons are computational, as discussed below in §3.4, and relate to computational times required to exhaustively explore a 10-dimensional parameter space. More generically, when stable steady structures occur transient solutions only converge at long times (often also related to the initial conditions). In marginal cases separating stable and unstable states, convergence times become infinite and transient simulations are frequently quite simply inappropriate to determine marginal conditions with any accuracy. This motivates the development of a semi-analytical approach, presented below in §4. In this approach we first reduce the problem to one dimension, so that computational simulations are indeed feasible. Second, we reduce the parametric dependence of the model from 10 dimensionless parameters to eight. Finally, this simplified approach allows analytical determination of conditions for steady-state displacements.

3.4. *Computational issues*

Finally, we mention some problems with the two-dimensional simulation method. First, some spreading of the interface does occur. We start the computations with a jump in $\bar{c}$ across the interface, but a small diffuse region emerges immediately. Although we have considered $\bar{c} = 0.5$ as the interface, this is arbitrary and any other contour could be used, giving rise to some uncertainty in computed interface position. The spreading is due partly to numerical diffusion, partly to dispersion and partly to interpolation errors. The FCT scheme is reasonable in regard to numerical diffusion but cannot eliminate this effect. We see that in the moving frame of reference there are significant counter-current secondary flows close to the interface. These act to amplify any spreading via dispersion, but the size of the effect is hard to quantify. Similarly, it is necessary to provide closure functions for the physical properties of the fluids. Here we have followed Bittleston *et al.* (2002) and used linear interpolation. Effects of using different closure laws are unknown. An obvious solution to these numerical issues would be to use an interface tracking method directly. We do this below for a simplified model, but have not tried to use it with the two-dimensional model.

Secondly, although by comparison to other problems routinely solved in fluid mechanics, the computational load for a two-dimensional problem may seem low, it is not so when yield stress fluids are involved (which is a situation of practical interest). The Uzawa algorithm used to solve the augmented Lagrangian problem converges relatively slowly and this must be repeated at each time step. Run times are still several hours on a 2007 desktop PC. This is sufficient to dissuade us from extensive explorations of parameter space. Linked to the above point, we may observe that

many of the flows we have computed do have interfaces that extend significantly along the annulus axis. Evidently, these elongated interfaces lead to larger computational domains and thus slower computational times. The approach that we explore below in §4 is an analytical effort to circumvent some of these difficulties. It might also be possible to look at improved computational techniques, such as adaptive meshing (note that much of the flow away from the front is one-dimensional), or implementing a parallel algorithm. So far we have not investigated these approaches.

4. A lubrication model for gravitational spreading with $|\tilde{b}| \gg 1$

We have seen that both positive and negative $\tilde{b}$ can lead to both steady travelling wave displacements and to unsteady displacements. Here we attempt to provide a quantitative understanding of these phenomena through analysis of the lubrication/thin-film limit, $|\tilde{b}| \gg 1$, which we derive below.

4.1. *Lubrication model derivation*

When $|\tilde{b}| \gg 1$ the buoyancy tends to dominate and causes the interface to elongate in the axial direction. We adopt the interface tracking formulation of §2.1, and introduce a small parameter $\varepsilon = 1/|\tilde{b}| \ll 1$. We will consider only mechanically stable configurations, i.e. if $\tilde{b} < 0$ it is assumed that the displacing fluid elongates along the bottom of the annulus (narrow side), and if $\tilde{b} > 0$ the elongation is along the top of the annulus (wide side). Only the model with $\tilde{b} < 0$ is derived; $\tilde{b} > 0$ is stated afterwards.

We assume that $|\tilde{b}|$ represents the length scale in the axial direction over which the streamlines, interface and modified pressure gradient field are all pseudo-parallel, and make the following assumptions.

(i) *Streamlines are pseudo-parallel to the annulus axis:* so that the main velocity component is in the ξ-direction, and hence

$$\left|\frac{\partial \Psi}{\partial \xi}\right| = O(\varepsilon), \qquad \left|\frac{\partial \Psi}{\partial \phi}\right| = O(1). \tag{4.1}$$

(ii) *Interface is pseudo-parallel to the annulus axis:* i.e. is highly elongated in the ξ-direction. Denoting the interface by $\phi = \phi_i(\xi, t)$ this translates into

$$\left|\frac{\partial \phi_i}{\partial \xi}\right| = O(\varepsilon). \tag{4.2}$$

(iii) *Modified pressure gradient field:* $\boldsymbol{S}_k$ has its main component in the ϕ-direction, driving the flow axially:

$$|S_{k,\xi}| = O(\varepsilon), \qquad |S_{k,\phi}| = O(1). \tag{4.3}$$

Note that this follows directly from (i) and the definition of $\boldsymbol{S}$ in the case that the fluids are yielded. Otherwise this is an additional assumption.

With the above assumptions, we re-scale axial length and time variables by

$$z = \varepsilon \xi, \qquad \tilde{t} = \varepsilon t. \tag{4.4}$$

For the velocity and pressure we set

$$W = \overline{w}, \qquad V = \varepsilon \overline{v}, \qquad P = \varepsilon p, \tag{4.5}$$

and write $\Psi(\phi, z)$ for the stream function as before. Note that $V = -\Psi_z = O(1)$ following this re-scaling.

After some manipulation, see Pelipenko & Frigaard (2004*c*), the kinematic equation for the interface $\phi = \phi_i(z, \tilde{t})$ becomes

$$\frac{\partial}{\partial \tilde{t}}\left[\int_0^{\phi_i(z,\tilde{t})} H(\phi)\,\mathrm{d}\phi\right] + \frac{\partial}{\partial z}[\Psi(\phi, z, \tilde{t})|_{\phi=\phi_i(z,\tilde{t})}] = 0. \tag{4.6}$$

The first term above is the time derivative of the *volumetric* interface position, $\Phi_i(z, \tilde{t})$:

$$\Phi_i(z, \tilde{t}) = \int_0^{\phi_i(z,\tilde{t})} H(\phi)\,\mathrm{d}\phi = \phi_i(z, \tilde{t}) + \frac{e}{\pi}\sin \pi\phi_i(z, \tilde{t}), \tag{4.7}$$

i.e. $\Phi_i(z, \tilde{t})$ represents the volume fraction of fluid 1 at depth z. The relationship between ϕ_i and Φ_i is linear, so we may write $\phi_i = \phi_i(\Phi_i)$.

The components of $\boldsymbol{S}_k$ are given in terms of the pressure and gravitational acceleration by

$$S_{k,\phi} = -\frac{\partial p}{\partial \xi} - \frac{\rho_k \cos\beta}{St^*}, \qquad S_{k,\xi} = \frac{\partial p}{\partial \phi} - \frac{\rho_k \sin\beta \sin \pi\phi}{St^*}.$$

The assumption that $|S_{k,\xi}| = O(\varepsilon)$ implies that

$$\frac{1}{\varepsilon}\left[\frac{\partial P}{\partial \phi} - \frac{\rho_k \sin\beta \sin \pi\phi}{\rho_1 - \rho_2}\right] = O(\varepsilon),$$

and we shall assume that $\beta \sim \pi/2 + O(\varepsilon)$, so that to $O(\varepsilon^2)$:

$$P(\phi, z, \tilde{t}) = \begin{cases} P(0, z, \tilde{t}) + \dfrac{\rho_2}{\pi(\rho_1 - \rho_2)}[1 - \cos \pi\phi], & \phi \in [0, \phi_i], \\ P(0, z, \tilde{t}) + \dfrac{\rho_2}{\pi(\rho_1 - \rho_2)}\left[1 - \dfrac{\rho_1}{\rho_2}\cos \pi\phi\right] + \dfrac{\cos \pi\phi_i}{\pi}, & \phi \in (\phi_i, 1]. \end{cases} \tag{4.8}$$

We write $\cos\beta = \alpha\varepsilon$ with $\alpha = O(1)$ so that

$$S_{1,\phi} = -\frac{\partial P}{\partial z}(0, z, \tilde{t}) - \frac{\rho_1 \alpha}{\rho_1 - \rho_2} + \frac{\partial \phi_i}{\partial z}\sin \pi\phi_i,$$
$$S_{2,\phi} = -\frac{\partial P}{\partial z}(0, z, \tilde{t}) - \frac{\rho_2 \alpha}{\rho_1 - \rho_2}.$$

Note that $S_{1,\phi} = S_{2,\phi} - (\alpha - \phi_{i,z}\sin \pi\phi_i)$ and that each $S_{k,\phi}$ is independent of ϕ.

In order to find the stream function at each $(z, \tilde{t})$, we need only find $A(z, \tilde{t}) = S_{2,\phi}$, which we do by using the boundary condition at $\phi = 1$ and the closure laws for the individual fluid phases:

$$1 = \Psi(1, z, \tilde{t}) = \int_0^{\phi_i} \left.\frac{\partial \Psi}{\partial \phi}\right|_{k=2} \mathrm{d}\phi + \int_{\phi_i}^1 \left.\frac{\partial \Psi}{\partial \phi}\right|_{k=1} \mathrm{d}\phi. \tag{4.9}$$

To evaluate the integrands, from (2.9) we have in fluid 1

$$\left.\frac{\partial \Psi}{\partial \phi}\right|_{k=1} = \mathrm{sgn}(A-b)\begin{cases} 0, & |A-b| \leqslant \tau_{1,Y}/H, \\ \dfrac{H^{m_1+2}}{\kappa_1^{m_1}(m_1+2)}\dfrac{(|A-b| - \tau_{1,Y}/H)^{m_1+1}}{|A-b|^2}\left[|A-b| + \dfrac{\tau_{1,Y}/H}{m_1+1}\right], & |A-b| > \tau_{1,Y}/H, \end{cases} \tag{4.10}$$

where $b = \alpha - \phi_{i,z} \sin \pi\phi_i$, and in fluid 2

$$\left.\frac{\partial \Psi}{\partial \phi}\right|_{k=2} = \operatorname{sgn}(A) \begin{cases} 0, & |A| \leqslant \tau_{2,Y}/H, \\ \dfrac{H^{m_2+2}}{\kappa_2^{m_2}(m_2+2)} \dfrac{(|A| - \tau_{2,Y}/H)^{m_2+1}}{|A|^2} \left[|A| + \dfrac{\tau_{2,Y}/H}{m_2+1}\right], & |A| > \tau_{2,Y}/H. \end{cases} \tag{4.11}$$

Both (4.10) and (4.11) are monotone with respect to A, and from this we can deduce that (4.9) has a unique solution. For the general case, this solution must be determined numerically.

Having found A, we may integrate to find Ψ. Replacing ϕ_i with $\phi_i(\Phi_i)$, we see that Ψ depends on $(z, \tilde{t})$ only via $\Phi_i(z, \tilde{t})$ and b, which contains $\Phi_i(z, \tilde{t})$ and $\Phi_{i,z}(z, \tilde{t})$. The value of the stream function at the interface is denoted by

$$q(\Phi_i, b) = \Psi(\phi, \phi_i, b)|_{\phi=\phi_i(z,\tilde{t})} : \quad b = \alpha - \phi_{i,z} \sin \pi\phi_i, \quad \phi_i = \phi_i(\Phi_i(z, \tilde{t})). \tag{4.12}$$

Using this notation, (4.6) yields an evolution equation for the propagation of the volumetric interface position, $\Phi_i(z, \tilde{t})$:

$$\frac{\partial \Phi_i}{\partial \tilde{t}} + \frac{\partial}{\partial z} q(\Phi_i, b) = 0. \tag{4.13}$$

4.2. *Diffusive nature of (4.13)*

Equation (4.13), with fixed constant b, is exactly the lubrication displacement flow conservation law studied in Pelipenko & Frigaard (2004*c*). This is a first-order quasi-linear, partial differential equation that admits a variety of different qualitative behaviours, including shocks and travelling wave solutions. Note that $b = \alpha - \phi_{i,z} \sin \pi\phi_i$ and hence (4.13) is second order and can be written as

$$\frac{\partial \Phi_i}{\partial \tilde{t}} + \left(\frac{\partial q}{\partial \Phi_i} + \frac{\partial q}{\partial b}\frac{\partial b}{\partial \Phi_i}\right)\frac{\partial \Phi_i}{\partial z} = -\frac{\partial q}{\partial b}\frac{\partial b}{\partial \Phi_{i,z}}\frac{\partial^2 \Phi_i}{\partial z^2}, \tag{4.14}$$

where

$$\frac{\partial b}{\partial \Phi_{i,z}} = -\frac{\sin \pi\phi_i}{1 + e \cos \pi\phi_i} < 0, \qquad \Phi_i \in (0, 1).$$

Therefore (4.13) will be diffusive only if q is non-decreasing for all b. This is the case, as might be expected physically, i.e. gravity should act to spread the interface along the annulus. We expect that the effects of diffusion will be to smooth out sharp changes in interface shape, e.g. the shocks found for the first-order model in Pelipenko & Frigaard (2004*c*), but it is interesting that on wide and narrow sides of the annulus the diffusion terms vanish.

LEMMA 1. *$q(\Phi_i, b)$ is non-decreasing for all b.*

Proof. See Appendix B.

4.3. *Steady travelling wave solutions*

Probably the single most important feature of (4.13) to predict is whether or not steady travelling wave solutions can be found, since in their absence it is likely that the flow will stratify, implying the ineffectiveness of the displacement. Since horizontal well sections are constructed to lie along the reservoir, failure of a horizontal cemented section has a large impact on well productivity. We show that it is in fact possible

to predict the conditions under which a steady travelling wave solution can be found.

It is more convenient to work in a moving frame of reference and (due to the scaling adopted) a steady travelling wave solution that occupies the entire annulus will move with unit speed. Thus, we write $x = z - t$ and seek a steady profile $\Phi_i = \Phi_i(x)$. For heavy fluids displacing light fluids ($\tilde{b} < 0$), we expect an interface shape as illustrated schematically in figure 2(*a*), so that $\Phi_i(x)$ is non-decreasing. Writing instead $x = x(\Phi_i)$ for the steady state, we seek $x(\Phi_i)$ such that the following physical conditions are satisfied:

$$\left.\begin{array}{ll} x'(0) = 0, & x''(0) > 0, \\ x'(1) = 0, & x''(1) < 0, \\ x'(\Phi_i) > 0 & \Phi_i \in (0,1). \end{array}\right\} \tag{4.15}$$

Substituting for $\Phi_i = \Phi_i(x)$ in the evolution equation (4.13) we find

$$\frac{\mathrm{d}}{\mathrm{d}x}[q\left(\Phi_i, b(\Phi_i, \Phi_i')\right) - \Phi_i] = 0,$$

and hence

$$q\left(\Phi_i, b(\Phi_i, \Phi_i')\right) - \Phi_i = 0 \tag{4.16}$$

must be satisfied by $\Phi_i(x)$ (or $x(\Phi_i)$). Since

$$b = \alpha - \phi_{i,z}\sin\pi\phi_i = \alpha - \frac{\sin\pi\phi_i(\Phi_i)}{H(\phi_i(\Phi_i))}\Phi_i'(x) = \alpha - \frac{\sin\pi\phi_i(\Phi_i)}{H(\phi_i(\Phi_i))x'(\Phi_i)},$$

we see that equation (4.16) is in fact an algebraic equation for the derivative, $x'(\Phi_i)$, of $x(\Phi_i)$ with respect to Φ_i.

Evidently, we can integrate $x'(\Phi_i)$ to give the steady-state shape provided that for all $\Phi_i \in [0, 1]$ there is a b for which (4.16) is satisfied and for which the conditions (4.15) on the physical shape of the interface are also satisfied. Since $q(\Phi_i, b)$ is continuous with respect to both arguments, this suffices to give a steady-state shape.

Theorem 1. *The condition that*

$$q(\Phi_i, \alpha) \geqslant \Phi_i \quad \textit{for all } \Phi_i \in [0,1] \tag{4.17}$$

is a necessary and sufficient condition for the existence of a steady-state travelling wave solution satisfying the conditions (4.15).

Proof. First recall from Lemma 1 that $q(\Phi_i, b)$ increases monotonically with respect to b. Therefore, if $\Phi_i \in (0, 1)$, from (4.15) we observe that $\alpha > b$. Additionally, as $\Phi_i \to 0$

$$b \to \alpha - \frac{\pi}{(1+e)^2 x''(0)} + O(\Phi_i) < \alpha$$

and as $\Phi_i \to 1$

$$b \to \alpha + \frac{\pi}{(1-e)^2 x''(1)} + O(\Phi_i) < \alpha.$$

Therefore $b < \alpha$ for all $\Phi_i \in [0, 1]$ and Lemma 1 implies that

$$q(\Phi_i, b) \leqslant q(\Phi_i, \alpha) \quad \text{for all } \Phi_i \in [0,1].$$

Thus, condition (4.17) is certainly a necessary condition to find a solution of (4.16).

For sufficiency, let $q(\Phi_i, b)$ be given by (4.9)–(4.12) and suppose that (4.15) and (4.17) are satisfied. We shall now find $b < \alpha$ such that $q(\Phi_i, b) = \Phi_i$. For fixed $\Phi_i \in [0, 1]$ define

$$g_L(\tilde{A}) = \int_0^{\phi_i} \partial\Psi/\partial\phi|_2 \, \mathrm{d}\phi \quad \text{and} \quad g_H(\tilde{A}) = \int_{\phi_i}^1 \partial\Psi/\partial\phi|_1 \, \mathrm{d}\phi,$$

i.e. we use (4.11) with A replaced by $\tilde{A}$ for $g_L(\tilde{A})$, and (4.10) with $A - b$ replaced by $\tilde{A}$ for $g_H(\tilde{A})$. We note that $\partial\Psi/\partial\phi$ in (4.10) and (4.11) increases continuously and monotonically with the modified pressure gradient $\tilde{A}$, approaching $\pm\infty$ as $\tilde{A} \to \pm\infty$. This monotonicity transfers to g_H and g_L. Using the monotonicity of g_H and g_L, for any fixed α it follows that there is an $\tilde{A}$ such that

$$g_L(\tilde{A}) + g_H(\tilde{A} - \alpha) = 1.$$

This is the procedure for defining $q(\Phi_i, \alpha) = g_L(\tilde{A})$ and, since (4.17) is satisfied,

$$g_L(\tilde{A}) \geqslant \Phi_i \quad \text{and} \quad g_H(\tilde{A} - \alpha) \leqslant 1 - \Phi_i.$$

Again from the monotonicity of g_H and g_L, it follows that we can find $A_L < \tilde{A}$ and $A_H > \tilde{A} - \alpha$ such that

$$g_L(A_L) = \Phi_i \quad \text{and} \quad g_H(A_H) = 1 - \Phi_i. \tag{4.18}$$

Now let b be defined by $b = A_L - A_H < \alpha$. Therefore

$$g_L(A_L) + g_H(A_L - b) = 1,$$

and by setting $g_L(A_L) = q(\Phi_i, b)$ we have a solution to (4.16). □

To understand the physical meaning of Theorem 1, note that $q(\Phi_i, b)$ is the volumetric flux through the upper layer of light fluid and $q(\Phi_i, \alpha)$ is the volumetric flux through the upper layer of light fluid, neglecting the effects of the interface slope. Condition (4.16) defines the distribution of volumetric flux for which the interface speed is everywhere identically equal to the mean speed of the flow. As the slope of the interface is positive and q increases with b, we can deduce that q decreases as the slope is increased. When condition (4.17) is satisfied, this implies that the flux is too large to satisfy (4.16). However, by increasing the slope of the interface from zero we can find a b for which (4.16) is satisfied. This constructive procedure gives the slope of the steady-state shape, as well as the conditions for there to be a steady state.

4.3.1. *Conditions on the consistency ratio*

The procedure in the above theorem can be made constructive and yields conditions on the consistency ratio, κ_1/κ_2, that need to be satisfied for a steady state to exist. First note that for a given modified pressure gradient $\tilde{A}$, (4.10) and (4.11) can be rewritten as

$$\frac{\partial\Psi}{\partial\phi}(\tilde{A}) = \mathrm{sgn}(\tilde{A}) \frac{|\tilde{A}|^m}{\kappa^m (m+2)} F_+(B, m, H(\phi)), \tag{4.19}$$

where

$$F_+(B, m, H) = \begin{cases} 0, & 1 \leqslant B/H, \\ \dfrac{H^{m+2}(1 - B/H)^{m+1}(1 + m + B/H)}{m+1}, & 1 > B/H. \end{cases} \tag{4.20}$$

$B = \tau_Y/|\tilde{A}|$ and in fluid k we use $m = m_k$, $\tau_Y = \tau_{Y,k}$, $\kappa = \kappa_k$. The only dependence on ϕ enters through the function $F_+(B, m, H)$.

For given Φ_i define A_L and A_H as

$$\frac{A_L^{m_2}}{\kappa_2^{m_2}(m_2+2)} I_L = \Phi_i \quad \text{and} \quad \frac{A_H^{m_1}}{\kappa_1^{m_1}(m_1+2)} I_H = 1-\Phi_i, \tag{4.21}$$

where

$$I_L = \int_0^{\phi_i} F_+(B_2, m_2, H(\phi))\, \mathrm{d}\phi \quad \text{and} \quad I_H = \int_{\phi_i}^1 F_+(B_1, m_1, H(\phi))\, \mathrm{d}\phi, \tag{4.22}$$

with $B_1 = \tau_{Y,1}/A_L$ and $B_2 = \tau Y, 2/A_H$. Thus if we set

$$b(\Phi_i) = \left(\frac{(m_2+2)\Phi_i}{I_L}\right)^{n_2} \kappa_2 - \left(\frac{(m_1+2)(1-\Phi_i)}{I_H}\right)^{n_1} \kappa_1, \tag{4.23}$$

we have that $q(\Phi_i, b) = \Phi_i$. Using the definition of b from (4.12)

$$x'(\Phi_i) = \frac{\sin \pi\phi_i(\Phi_i)}{H(\Phi_i)(\alpha - b(\Phi_i))}, \tag{4.24}$$

and we note that to be physically plausible we require $x'(\Phi_i) > 0$ for $\Phi_i \in (0,1)$, see the conditions (4.15). This implies that

$$\frac{\kappa_1}{\kappa_2} > \max_{\Phi_i \in [0,1]} F_{HL}(\Phi_i; e, n_1, n_2, B_1, B_2, \alpha/\kappa_2), \tag{4.25}$$

where

$$F_{HL} = \frac{\left(\dfrac{(m_2+2)\Phi_i}{I_L}\right)^{n_2}}{\left(\dfrac{(m_1+2)(1-\Phi_i)}{I_H}\right)^{n_1}} - \frac{\alpha}{\kappa_2} \frac{1}{\left(\dfrac{(m_1+2)(1-\Phi_i)}{I_H}\right)^{n_1}}, \tag{4.26}$$

and recall that $m_k = 1/n_k$. When condition (4.25) is satisfied, the shape of the steady travelling wave can be found by integrating (4.24).

4.4. *Light displacing fluids,* $\tilde{b} > 0$

When the displacing fluid is lighter than the displaced fluid we expect the configuration illustrated schematically in figure 2(*b*) to result, and again it is possible to derive a lubrication displacement model. The volumetric interface position, $\Phi_i(z, \tilde{t})$, again evolves according to

$$\frac{\partial \Phi_i}{\partial \tilde{t}} + \frac{\partial}{\partial z} q(\Phi_i, b) = 0, \tag{4.27}$$

where now

$$q(\Phi_i, b) = \int_0^{\phi_i} \left.\frac{\partial \Psi}{\partial \phi}\right|_{k=1} \mathrm{d}\phi,$$

and this is computed in a similar way. The ϕ components of $\boldsymbol{S}$ in each fluid are constants satisfying $S_{2,\phi} = S_{1,\phi} - b$. Defining $S_{1,\phi} = A$, equations (4.10) and (4.11) are replaced by

$$\left.\frac{\partial \Psi}{\partial \phi}\right|_{k=1} = \mathrm{sgn}(A) \begin{cases} 0, & |A| \leqslant \tau_{1,Y}/H, \\ \dfrac{H^{m_1+2}}{\kappa_1^{m_1}(m_1+2)} \dfrac{(|A| - \tau_{1,Y}/H)^{m_1+1}}{|A|^2} \left[|A| + \dfrac{\tau_{1,Y}/H}{m_1+1}\right], & |A| > \tau_{1,Y}/H, \end{cases} \tag{4.28}$$

in fluid 1, and in fluid 2 by

$$\left.\frac{\partial \Psi}{\partial \phi}\right|_{k=2} = \operatorname{sgn}(A-b) \begin{cases} 0, & |A-b| \leqslant \tau_{2,Y}/H, \\ \dfrac{H^{m_2+2}}{\kappa_2^{m_2}(m_2+2)} \dfrac{(|A-b|-\tau_{2,Y}/H)^{m_2+1}}{|A-b|^2} \left[|A-b| + \dfrac{\tau_{2,Y}/H}{m_2+1}\right], & |A-b| > \tau_{2,Y}/H, \end{cases} \tag{4.29}$$

where b is still given by

$$b = \alpha - \phi_{i,z} \sin \pi\phi_i.$$

The modified pressure gradient A is computed from

$$1 = \Psi(1, z, \tilde{t}) = \int_0^{\phi_i} \left.\frac{\partial \Psi}{\partial \phi}\right|_{k=1} \mathrm{d}\phi + \int_{\phi_i}^1 \left.\frac{\partial \Psi}{\partial \phi}\right|_{k=2} \mathrm{d}\phi. \tag{4.30}$$

4.4.1. *Diffusive spreading and steady-state profiles*

As before, we can show that $q(\Phi_i, b)$ is non-decreasing with b and that (4.27) is diffusive in nature. The methodology is similar to that used previously. The profile of the interface when the displacing fluid is lighter is expected to satisfy

$$\left.\begin{array}{ll} x'(0) = 0, & x''(0) < 0, \\ x'(1) = 0, & x''(1) > 0, \\ x'(\Phi_i) < 0 & \Phi_i \in (0, 1), \end{array}\right\} \tag{4.31}$$

which replaces (4.15). Under these assumptions, a necessary and sufficient condition for a steady state is that

$$q(\Phi_i, \alpha) \leqslant \Phi_i. \tag{4.32}$$

This is satisfied if

$$\frac{\kappa_1}{\kappa_2} > \max_{\phi_i \in [0,1]} F_{LH}(\phi_i; e, n_1, n_2, B_1, B_2, \alpha/\kappa_2), \tag{4.33}$$

where

$$F_{LH} = \frac{\left(\dfrac{(m_2+2)(1-\Phi_i)}{I_H}\right)^{n_2}}{\left(\dfrac{(m_1+2)\Phi_i}{I_L}\right)^{n_1}} + \frac{\alpha}{\kappa_2} \frac{1}{\left(\dfrac{(m_1+2)\Phi_i}{I_L}\right)^{n_1}}. \tag{4.34}$$

In this case I_L and I_H are defined as

$$I_H = \int_{\phi_i}^1 F_+(B_2, m_2, H(\phi))\, \mathrm{d}\phi \tag{4.35}$$

$$I_L = \int_0^{\phi_i} F_+(B_1, m_1, H(\phi))\, \mathrm{d}\phi. \tag{4.36}$$

Note that in this case an increase in α requires an increase in the consistency ratio.

4.5. *Parametric results*

Here we explore conditions (4.25) and (4.33) that dictate whether or not a steady travelling wave shape can be found. Note that the procedure leading to (4.25) and (4.33) is constructive and is fully explicit in the case that the fluids have no yield stress. When the fluids have a yield stress the same procedure can be followed, but since B_k depends on the modified pressure gradients this relationship is implicit.

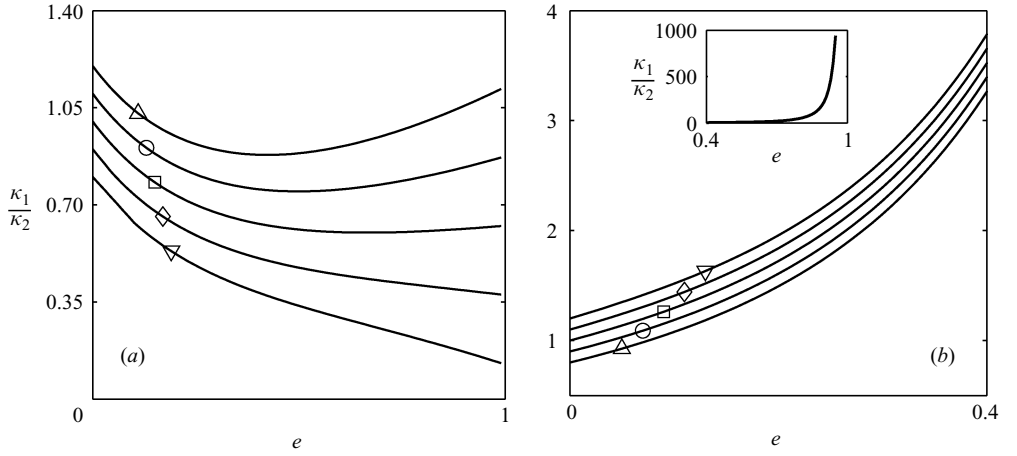

FIGURE 14. Conditions required for two Newtonian fluids to have a steady-state displacement: (*a*) HL - heavy fluid displacing light fluid, (4.26); (*b*) LH - light fluid displacing heavy fluid, (4.34). The curves are: $\alpha/\kappa_2 = -0.6$ (△), -0.3 (○), 0 (□), 0.3 (◇), 0.6 (▽). The consistency ratio must lie above the curve to have a steady travelling wave displacement.

4.5.1. *Newtonian fluids*

If the two fluids are Newtonian and the fluid 1 is heavier, the flux function q is

$$q_{HL}(\Phi_i, b) = \frac{\left(3\kappa_1 + b\int_{\phi_i}^{1} H^3(\phi)\mathrm{d}\phi\right)\int_0^{\phi_i} H^3(\phi)\mathrm{d}\phi}{3\kappa_2\int_{\phi_i}^{1} H^3(\phi)\mathrm{d}\phi + 3\kappa_1\int_0^{\phi_i} H^3(\phi)\mathrm{d}\phi}. \tag{4.37}$$

When the displacing fluid is lighter this expression becomes

$$q_{LH}(\Phi_i, b) = \frac{\left(3\kappa_2 + b\int_{\phi_i}^{1} H^3(\phi)\mathrm{d}\phi\right)\int_0^{\phi_i} H^3(\phi)\mathrm{d}\phi}{3\kappa_2\int_0^{\phi_i} H^3(\phi)\mathrm{d}\phi + 3\kappa_1\int_{\phi_i}^{1} H^3(\phi)\mathrm{d}\phi}. \tag{4.38}$$

The conditions required to have a steady state, (4.26) and (4.34), are plotted for different angles α in figure 14. Note that a positive angle helps the heavy–light (HL) displacement, while it worsens the light–heavy (LH) displacement.

In figure 15 the effects on the steady-state shape of increasing the eccentricity at fixed consistency ratio are illustrated. It is interesting to note that increasing the eccentricity has a different effect in an HL displacement than an LH displacement. In the former the density difference promotes slumping along the bottom of the well and an increase in eccentricity counters this effect by constricting the area. Increasing eccentricity acts to elongate the interface for the LH displacement.

The effects on the steady-state shape of increasing the consistency ratio at fixed eccentricity are shown in figure 16 for $e = 0.1$. In this case the consistency ratio threshold for the HL displacement is $\kappa_1/\kappa_2 = 0.8388$, while for the the LH displacement it is $\kappa_1/\kappa_2 = 1.2959$. In both cases the consistency ratios explored are above the threshold values and we can observe that increasing the consistency ratio tends to reduce the extension of the interface along the annulus. As the threshold value is approached the steady states elongate towards infinity, see e.g. figure 16(*b*).

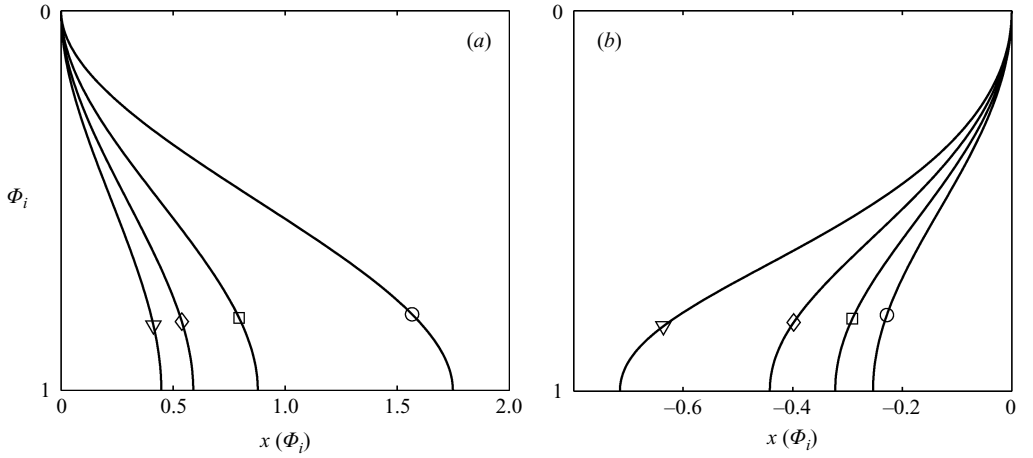

FIGURE 15. The effects on the steady-state shape of increasing the eccentricity at fixed consistency ratio for two Newtonian fluids: (*a*) HL displacement $\kappa_1/\kappa_2 = 1$; (*b*) LH displacement $\kappa_1/\kappa_2 = 2.02$. Eccentricities: $e = 0.05$ (○), 0.1 (□), 0.15 (◇), 0.2 (▽); horizontal well $\alpha/\kappa_2 = 0$.

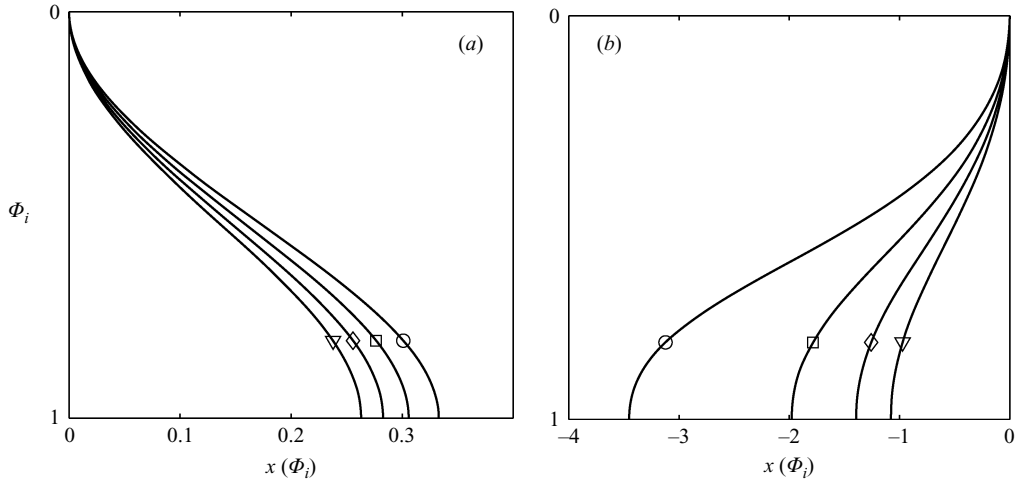

FIGURE 16. The effects on the steady-state shape of increasing the consistency ratio at fixed eccentricity, $e = 0.1$, for 2 Newtonian fluids: (*a*) HL displacement; (*b*) LH displacement. Consistency ratios: $\kappa_1/\kappa_2 = 1.35$ (○), 1.4 (□), 1.45 (◇), 1.5 (▽); horizontal well, $\alpha/\kappa_2 = 0$.

4.5.2. *Power-law fluids*

We investigate the effects of shear-thinning on steady displacements only for displacements in strictly horizontal wells, $\alpha = 0$. Figures 17 and 18 show the effects of varying power-law indices on the threshold consistency ratio. Figure 17 fixes $n_1 = 0.5$ and explores the effect of increasing eccentricity for different n_2. For HL displacements the threshold is either decreasing with e or has a minimum (see also the Newtonian case in figure 14), i.e. a little eccentricity helps the displacement countering the effects of buoyancy.

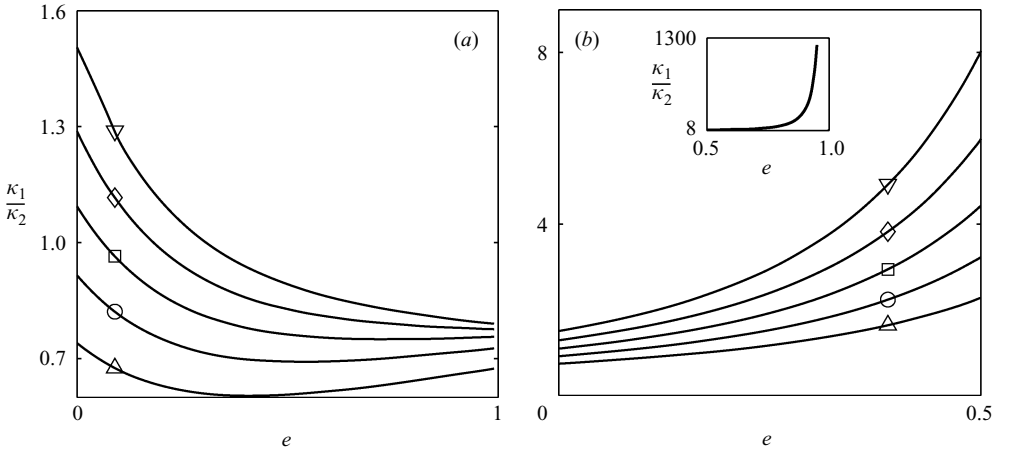

FIGURE 17. Conditions required to have a steady-state displacement at fixed $n_1 = 0.5$, for two power-law fluids: (*a*) HL displacement, (4.26); (*b*) LH displacement, (4.34). The curves are: $n_2 = 0.2$ (△), 0.4 (○), 0.6 (□), 0.8 (◇), 1.0 (▽). The consistency ratio must lie above the curve to have a steady displacement.

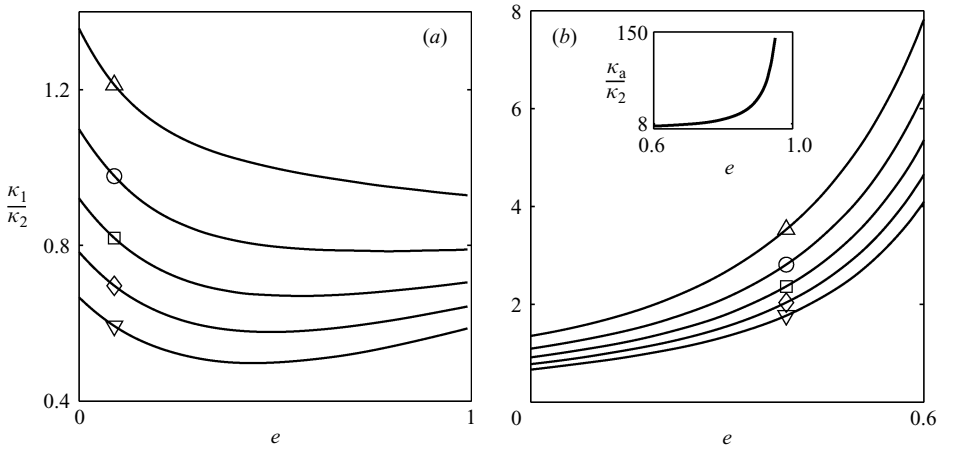

FIGURE 18. Conditions required to have a steady-state displacement at fixed $n_2 = 0.5$, for two power-law fluids: (*a*) HL displacement, (4.26); (*b*) LH displacement, (4.34). The curves are: $n_1 = 0.2$ (△), 0.4 (○), 0.6 (□), 0.8 (◇), 1.0 (▽). The consistency ratio must lie above the curve to have a steady displacement.

For LH displacements the consistency ratio increases with e. On increasing n_2, the power-law index of the displaced fluid in both cases increases the consistency ratio threshold. Essentially the displaced fluid is becoming more viscous. In general, comparing figures 17(*a*) and 17(*b*), the LH displacement requires a higher consistency ratio than the HL displacement in order to become steady. The results shown in figures 18 are qualitatively similar with respect to variations in e. Now, as n_1 is increased (for fixed n_2), the consistency ratio threshold drops. Again this can simply be interpreted as an increase in viscosity ratio.

The shape of the steady states is explored in figures 19 and 20. We fix $n_1 = 0.5, n_2 = 1$ and explore the effects of changing consistency ratio and eccentricity. Essentially, the

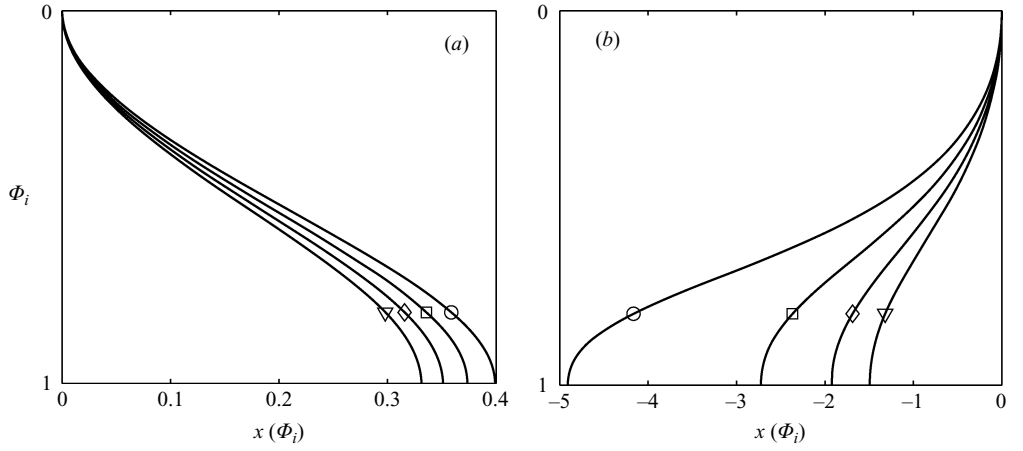

FIGURE 19. The effects on the steady-state shape of increasing the consistency ratio at fixed eccentricity and power-law indices, $e = 0.1$, $n_1 = 0.5$, $n_2 = 1$: (*a*) HL displacement: threshold $\kappa_1/\kappa_2 = 1.2637$; (*b*) LH displacement: threshold $\kappa_1/\kappa_2 = 1.9154$. Consistency ratios: $\kappa_1/\kappa_2 = 1.95$ (○), 2 (□), 2.05 (◇), 2.1 (▽); horizontal well, $\alpha/\kappa_2 = 0$.

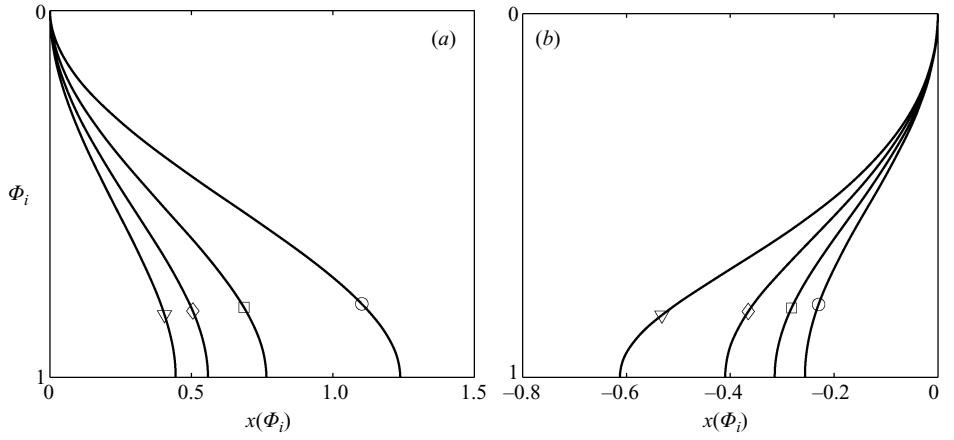

FIGURE 20. The effects on the steady-state shape of increasing the eccentricity at fixed consistency ratio and power-law indices, $n_1 = 0.5$, $n_2 = 1$: (*a*) HL displacement, $\kappa_1/\kappa_2 = 1.6$; (*b*) LH displacement, $\kappa_1/\kappa_2 = 2.97$. Eccentricities: $e = 0.05$ (○), 0.1 (□), 0.15 (◇), 0.2 (▽); horizontal well $\alpha/\kappa_2 = 0$.

steady-state shape becomes progressively elongated as the threshold is approached. The results for $n_1 = 1$, $n_2 = 0.5$ are analogous.

4.5.3. *Yield-stress fluids*

For yield-stress fluids we cannot get a closed-form expression for a critical consistency ratio, as B_1 and B_2 depend on the modified pressure gradient. Instead, we follow the procedure of Theorem 1. For example, for a HL displacement at each Φ_i we find $A_L(\Phi_i)$ and $A_H(\Phi_i)$ from (4.18). Provided that $A_L(\Phi_i) - A_H(\Phi_i) < \alpha$ for all $\Phi_i \in [0, 1]$ we can construct a steady-state shape. The critical condition is when

$$\max_{\Phi_i \in [0,1]} \{A_L(\Phi_i) - A_H(\Phi_i)\} = \alpha. \tag{4.39}$$

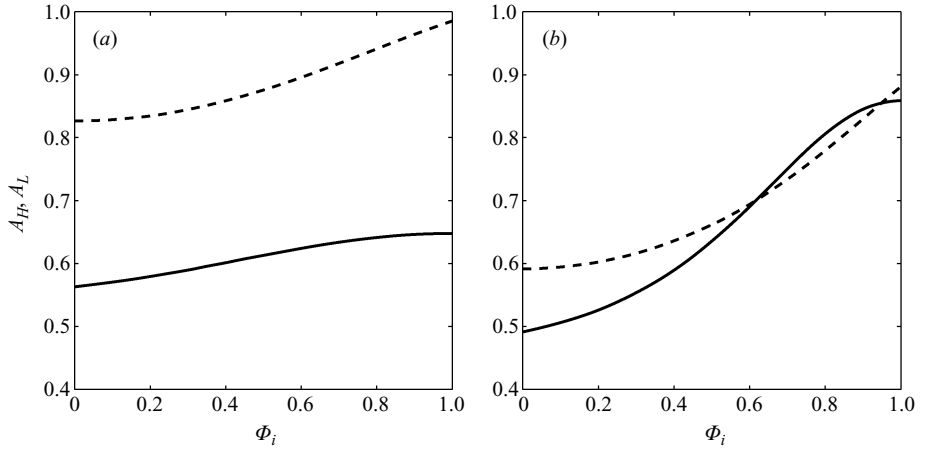

FIGURE 21. Examples of $A_L(\Phi_i)$ and $A_H(\Phi_i)$ for parameters $\tau_{Y,1} = 0.4$, $\kappa_1 = 0.1$, $n_1 = 0.5$, $\tau_{Y,2} = 0$, $\kappa_2 = 1$, $n_2 = 1$, $\alpha = 0$: (*a*) $e = 0.1$, steady state; (*b*) $e = 0.3$, no steady state. $A_H(\Phi_i)$ corresponds to the broken line.

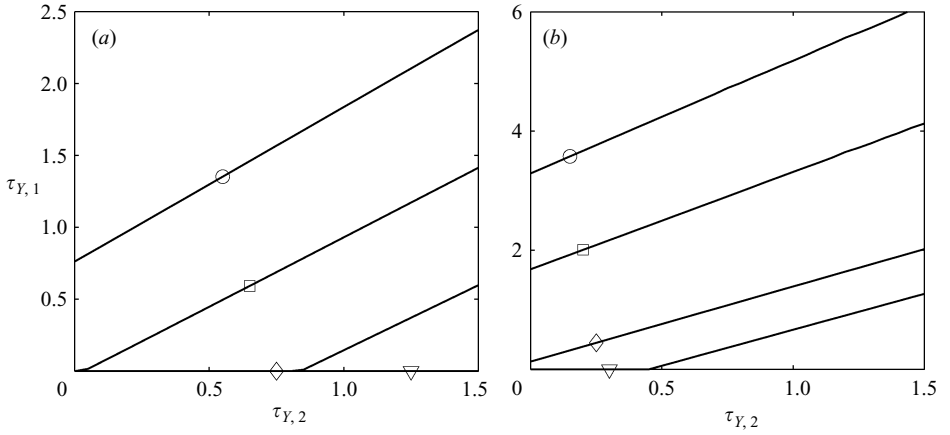

FIGURE 22. Conditions required to have a steady-state displacement at fixed: $n_1 = 0.5$, $n_2 = 0.8$, $e = 0.2$: (*a*) HL displacement (4.26); (*b*) LH displacement:(4.34). The curves are: $\kappa_1/\kappa_2 =$ 0.5 (○), 1.0 (□), 1.5 (◇), 2.0 (▽). The yield stress $\tau_{Y,1}$ must lie above the curve to have a steady displacement. Horizontal displacement $\alpha/\kappa_2 = 0$.

An analogous procedure is followed for LH displacements.

Two example computations of $A_L(\Phi_i)$ and $A_H(\Phi_i)$ are shown in figure 21. We may observe that in each case the functions $A_L(\Phi_i)$ and $A_H(\Phi_i)$ are monotone with respect to Φ_i. For the parameters of figure 21(*a*) it is possible to compute a steady-state shape, but for the parameters of figure 21(*b*) it is not. Evidently, computing the threshold in this way is not very efficient. However, figure 21 shows that the critical conditions may be met at an intermediate Φ_i, and therefore there does not appear to be any shortcut.

Figure 22 shows the conditions on $\tau_{Y,1}$ and $\tau_{Y,2}$ required in order to have a steady-state displacement, for parameters that are fixed otherwise. It is interesting to note that the marginal curves in the $(\tau_{Y,1}, \tau_{Y,2})$-plane are nearly linear. Example steady-state shapes are shown in figure 23.

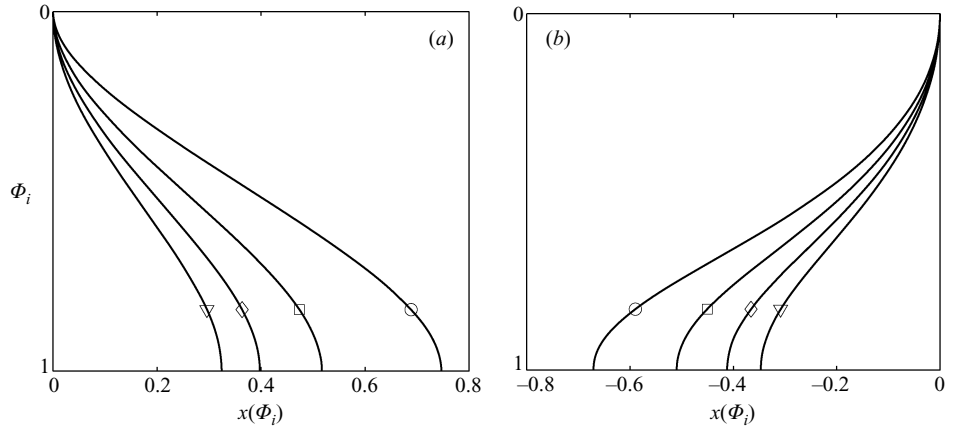

FIGURE 23. The effects on the steady-state shape of increasing the yield stress of the displacing fluid. $n_1 = 0.5$, $n_2 = 0.8$, $e = 0.2$, $\tau_{Y,2} = 0.5$: (*a*) HL displacement, $\alpha/\kappa_2 = 1.5$ (4.26); (*b*) LH displacement, $\alpha/\kappa_2 = 3.0$ (4.34). The curves are: $\tau_{Y,1} = 0$ (○), 0.25 (□), 0.5 (◇), 0.75 (▽). Horizontal displacement $\alpha/\kappa_2 = 0$

5. Discussion and summary

We have presented an analysis of displacement flows in horizontal eccentric annuli, in the Hele-Shaw limit, using two complementary models. Using a fully two-dimensional model and computational simulation we have studied a range of displacements involving either HL or LH fluid combinations. The role of density difference appears slightly different depending on whether the displacement is HL or LH. In the former case, density difference and eccentricity compete, so that there is often a threshold in the (St^*, e)-plane delineating steady and unsteady displacements. In LH displacement both eccentricity and buoyancy act to accentuate unsteadiness and stratification. However, in both cases we have seen that these flows may either stratify or displace in steady state.

For long computational domains, the two-dimensional model is less effective and more time consuming. This has motivated derivation of a one-dimensional lubrication-style displacement model. Interestingly, in this model we are able to decouple the effects of buoyancy from those of eccentricity and fluid rheology. For this simplified model we were able to give necessary and sufficient conditions for there to be a steady-state displacement, and have explored variations in the results with the main dimensionless parameters. In this model, fluid rheology and eccentricity alone determine whether or not there may be a steady state. The buoyancy force translates simply into an axial length scale for the slumped propagating steady interface, i.e. a larger density difference gives a longer axial extension to the steady state. We have presented the results for Newtonian and power-law fluids in terms of the ratio of consistencies of the two fluids: κ_1/κ_2. This must exceed a certain critical threshold in order for there to be a steady state. Above the threshold, steady-state shapes vary significantly with the other rheological parameters. The variation is fairly intuitive, i.e. as the displacing fluid is made more viscous the axial extent of the steady states decreases. Increasing eccentricity generally results in longer steady states. As the critical threshold is approached, the axial extent of the steady state grows towards infinity.

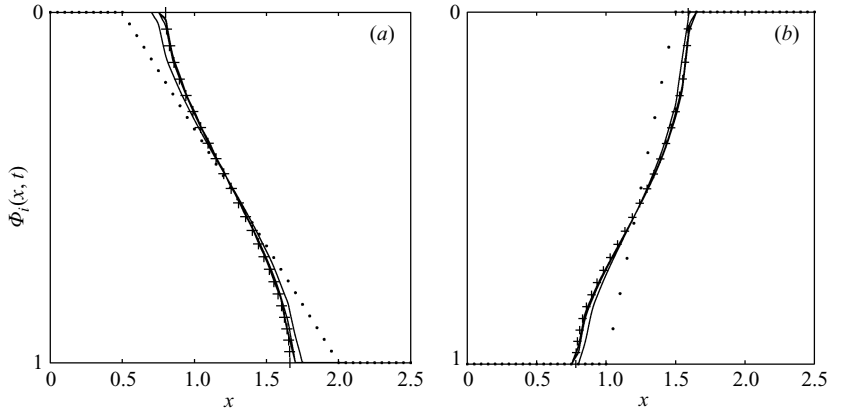

FIGURE 24. Examples of convergence to the steady-state profile for the lubrication displacement model. Parameters are: $e = 0.2$, $\tau_{Y,1} = 0$, $\tau_{Y,2} = 0$, $n_1 = 0.8$, $n_2 = 0.7$, $\alpha/\kappa_2 = 0$. (*a*) HL displacement, $\kappa_1/\kappa_2 = 0.8$; (*b*) LH displacement, $\kappa_1/\kappa_2 = 1.8$. Both examples have converged after approximately $t = 6$. In the figures, + is the steady-state profile, · the initial condition and the solid lines are transient profiles, evenly spaced in time.

5.1. *Steady state stability*

A question that is unanswered concerns the stability of the steady states. In the two-dimensional simulations, we only observe steady-state solutions that are stable, since they are identified via a transient computation. For the lubrication model we have a semi-analytic expression for the steady-state shape, but *a priori* there is no reason to expect that these shapes are stable. Nevertheless, numerical simulations with the lubrication model do indicate that the steady states are stable. An example of one such computation is shown in figure 24.

We have not been able to develop any simple stability analysis that predicts the stability of the steady states, but it appears that they are generally stable and perhaps globally so. This appears strange at first glance, in particular when one considers the moving-frame streamline pattern, $\Phi(x, \phi)$, for a steady-state displacement, as shown schematically in figure 25(*a*), (see also earlier results from the two-dimensional simulation). The steady state is a streamline $\Phi(x, \phi) = 0$ that connects wide and narrow sides of the annulus. The Hele-Shaw formulation allows a discontinuity in tangential velocity across an interface, and we see that the steady state has fluids 1 and 2 are counter-current on either side of it. Since the interface is advected by the velocity field, this configuration intuitively appears to be unstable to any small perturbation of the interface.

However, the above conclusion is based on the false assumption that the streamline field is not also perturbed by the interface perturbation, i.e. the transient interface is advected by the velocity field defined by the moving-frame streamfunction: $\Phi = \Phi(x, \phi, t, \Phi_i(x, t))$. From the two-dimensional simulations, we have seen that the approach to the steady state is characterized by the existence of a slowly counter-rotating zone about the interface, see figure 25(*b*), which contracts as the steady state is approached. With the streamlines and interface as in figure 25(*b*), we can see that the interface will remain within the circulatory region, with the two endpoints approaching points A and B, which are stable, and the interface being suspended between these two points. The steady-state streamline field is the limiting case in which such a (stabilizing) recirculation zone collapses to a line. The above appears to

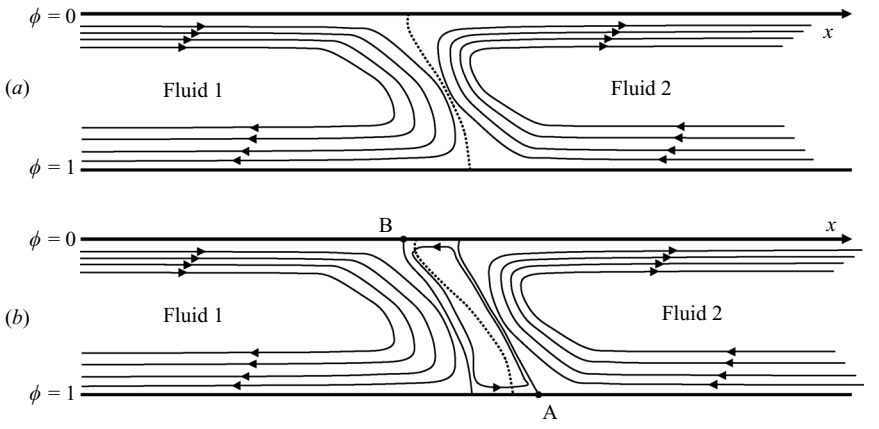

FIGURE 25. (*a*) Schematic of the streamlines for, a steady state and (*b*) when close to the steady state. The interface is shown schematically as the thick dotted line.

be the mechanism by which steady states are stable. This type of stability is likely to be nonlinear, but it is unclear if it is global.

5.2. *Industrial implications*

From the industrial perspective, the results of the paper are slightly counter-intuitive but have largely positive implications. They also fill a large gap in industrial understanding of these flows, where there is essentially no published analysis of the displacement mechanics. The three key contributions of the work are as follows.

(*a*) Eccentricity and density difference play the dominant roles in vertical annulus displacements. It has long been thought that in horizontal annuli density differences must be detrimental to a good displacement. We see that this is not entirely the case. In fact (at least in the lubrication limit), whether or not there is steady-state displacement in a horizontal well does not appear to be dictated by the density of the fluids. Rheology plays the dominant role in this question, regardless of the density difference.

(*b*) On the other hand, density difference does affect the length of the steadystate displacement profile, scaling linearly with density difference (divided by Stokes number). This scaling is evident in results from the two-dimensional computations (compare e.g. figures 6–8), and is implicit in the scaling adopted for the lubrication model. For two Newtonian fluids the Stokes number captures all the effects of pump flow rate, i.e. increasing $\hat{Q}$ reduces St^* in proportion to $1/\hat{Q}$. Thus, density difference and flow rate act counter to one another in determining the length of the displacement profile. For non-Newtonian fluid displacements, the flow rate affects the dimensionless rheological parameters so that it is harder to assess effects of flow rate.

(*c*) Criteria for the existence of a steady-state displacement have been developed and presented as either a critical consistency ratio, or other thresholds. It is relatively simple/quick to compute these criteria and this could easily be included as part of a design process. Given the apparent stability of these solutions, they are obviously of industrial interest.

Apart from the semi-analytical expressions given, which need minimal computing to evaluate, it would be of use to give some clear 'rules' that may be followed in industrial design. In this context, the construction leading to figure 21 is useful. For the HL-displacement, $A_L(\Phi_i)$ represents the pressure gradient required to move the

light fluid at mean speed through a duct consisting only of light fluid in the section $\phi \in [0, \Phi_i]$. Similarly, $A_H(\Phi_i)$ represents the pressure gradient required to move the heavy fluid at mean speed through a duct consisting only of heavy fluid in the section $\phi \in [1 - \Phi_i, 1]$. Conditions for which there can be no steady state are given (for $\alpha = 0$) by when $A_L(\Phi_i)$ and $A_H(\Phi_i)$ intersect. Sufficient conditions for this may be stated in terms of single-fluid hydraulic quantities as follows.

THEOREM 2. *For a displacement in a horizontal well, there will be no steady-state displacement if either of the following two sets of conditions are satisfied.*

(*a*) $\Delta P_{L,W} < \overline{\Delta P}_H$ *and* $\overline{\Delta P}_L > \Delta P_{H,N}$;

(*b*) $\Delta P_{L,W} > \overline{\Delta P}_H$ *and* $\overline{\Delta P}_L < \Delta P_{H,N}$.

Here $\Delta P_{L,W}$ denotes the frictional pressure drop generated when pumping the light (L) fluid through a concentric annulus of the same gap width as the wide (W) side at the imposed mean velocity; $\overline{\Delta P}_H$ denotes the frictional pressure drop generated when pumping the heavy (H) fluid through the eccentric annulus as the mean imposed speed; $\overline{\Delta P}_L$ denotes the frictional pressure drop generated when pumping the light (L) fluid through the eccentric annulus at the mean imposed speed; $\Delta P_{H,N}$ denotes the frictional pressure drop generated when pumping the heavy (H) fluid through a concentric annulus of the same gap width as the narrow (N) side at the imposed mean velocity.

Finally, when we do not have a steady-state displacement, or when the displacement front is steady but elongated, the flow streamlines are approximately pseudo-parallel. The stability of this type of parallel flow, within the Hele-Shaw context, has been recently studied in Moyers-Gonzalez & Frigaard (2007*a, b*). The results are too complex to summarize, but it is found that many such parallel flows are linearly unstable. Therefore, although potentially problematic from the industrial perspective, instability and subsequent mixing of the fluids azimuthally may make even these displacements acceptable, i.e. the mixing may prevent development of a long finger on the wide side. Equally, we have not considered situations in which a finger develops that is mechanically unstable (i.e. heavy fluid over light fluid). Although possible in our Hele-Shaw model, such configurations are likely to destabilize (again see Moyers-Gonzalez & Frigaard 2007*a, b*) for instability of the parallel flow).

Parts of this research have been carried out at the University of British Columbia, supported financially by Schlumberger and NSERC through CRD project 245434 and through Strategic Project Grant 306682-04. This support is gratefully acknowledged. We thank Mr Sardar Malekmohammadi for providing figure 3. We thank the referees for their constructive comments.

Appendix A. Model of the Flow of a Herschel–Bulkley Fluid

For a complete model derivation the reader is referred to Bittleston *et al.* (2002). In outline, we use classical Hele-Shaw scaling arguments to simplify the momentum equations to the following reduced shear flow:

$$\frac{\partial p}{\partial \phi} = \frac{\partial}{\partial y}\tau_{\phi y} + g_\phi \quad \text{and} \quad \frac{\partial p}{\partial \xi} = \frac{\partial}{\partial y}\tau_{\xi y} + g_\xi,$$

where y denotes a normalized annular gap coordinate, (v, w) are the azimuthal and axial velocity components, p is the pressure and (g_ϕ, g_ξ) denotes the scaled gravitational acceleration vector. The fluid rheology is assumed to be that of a

Herschel–Bulkley fluid:

$$\tau_{ij} = (\kappa \dot{\gamma}^{n-1} + \tau_Y/\dot{\gamma})\dot{\gamma}_{ij} \Leftrightarrow \tau > \tau_Y\,; \dot{\gamma} = 0 \Leftrightarrow \tau \leqslant \tau_Y.$$

After scaling only the leading-order shear stress and strain rate components (ϕy and ξy) are considered in the rheological law. The rheological parameters are defined as functions of the base fluid parameters and fluid concentration. It follows that the gap-averaged velocity flows in the direction of the modified pressure gradient,

$$\left(-\frac{\partial p}{\partial \phi} + g_\phi, -\frac{\partial p}{\partial \xi} + g_\xi\right)$$

and by orienting in the direction of this flow we may compute the relation (2.9) between mean flow rate and modified pressure gradient by solving a one-dimensional flow problem across the annular gap. Cross-differentiation to eliminate the pressure results in (2.4). For example, for a Newtonian fluid we recover the familiar $\boldsymbol{S} = 3\kappa\nabla\Psi/H^3$, and (2.4) is simply a linear elliptic equation driven by the buoyancy gradient and imposed flow rate.

Appendix B. Proof of Lemma 1

Proof. For brevity, let us write $u(\phi) = \Psi(\phi, z, t)$, $u'(\phi) = \partial\Psi/\partial\phi$, and observe that $u(\phi_i(\Phi_i)) = q(\Phi_i, b)$. We proceed formally by assuming that $u \in \mathscr{V}$, where $\mathscr{V}$ is a suitable function space for what follows. (Following Pelipenko & Frigaard (2004*a*) we can expect that $u \in W^{1,p}([0,1])$ with $p = \min\{1+n_1, 1+n_2\}$. However, their results are for a general two-dimensional flow, whereas here the base flows solved to give the lubrication model are one-dimensional. It is thus likely that the solution is piecewise C^1 (or smoother) and hence $H^1([0,1])$ could be used.) Note that $u(\phi)$ satisfies boundary conditions $u(0) = 0$ and $u(1) = 1$. We denote by $\mathscr{V}_0$ the subspace of $\mathscr{V}$ containing all functions $w(\phi) \in \mathscr{V}$ that satisfy homogeneous boundary conditions: $w(0) = w(1) = 0$. Then if u is the stream function solution, any other (test) solution $v \in \mathscr{V}$ can be written as

$$v = u + w, \quad \text{for some } w \in \mathscr{V}_0.$$

For $v \in \mathscr{V}$, we multiply the modified pressure gradients $S_{k,\phi}$ by $(u-v)'$ and integrate over $\phi \in [0,1]$. First, by using the definition of A and b we arrive at

$$\begin{aligned}\int_0^{\phi_i} (v-u)' S_{2,\phi}\,\mathrm{d}\phi + \int_{\phi_i}^1 (v-u)' S_{1,\phi}\,\mathrm{d}\phi &= \int_0^{\phi_i} (v-u)' A\,\mathrm{d}\phi + \int_{\phi_i}^1 (v-u)'(A-b)\,\mathrm{d}\phi \\ &= b\,(v(\phi_i) - u(\phi_i))\,. \end{aligned} \tag{B 1}$$

Considering first fluid 2, if fluid 2 is yielded we can use equation (2.7) directly to give

$$\begin{aligned}\int_0^{\phi_i} (v-u)' S_{2,\phi}\,\mathrm{d}\phi &= \int_0^{\phi_i} \left(\frac{\chi_2 + \tau_{2,y}/H}{|u'|}\right)(v-u)'u'\,\mathrm{d}\phi \\ &\leqslant \int_0^{\phi_i} \frac{\chi_2}{|u'|}(v-u)'u'\,\mathrm{d}\phi + \int_0^{\phi_i} \frac{\tau_{2,y}}{H}\left(|v'| - |u'|\right)\,\mathrm{d}\phi \end{aligned} \tag{B 2}$$

with the last step following from the Cauchy–Schwarz inequality. Note that when unyielded we have that $|S_{2,\phi}| \leqslant \tau_{2,y}/H$, $u' = 0$ and $\chi_2(|u'|) \to 0$ like $|u'|^{1/(1+1/n_2)}$ (see Pelipenko & Frigaard (2004*a*)). Therefore, inequality (B 2) is valid also if fluid 2 is

unyielded. We may write a similar inequality for fluid 1:

$$\int_{\phi_i}^{1}(v-u)'S_{1,\phi}\,\mathrm{d}\phi \leqslant \int_{\phi_i}^{1}\frac{\chi_1}{|u'|}(v-u)'u'\,\mathrm{d}\phi + \int_{\phi_i}^{1}\frac{\tau_{1,y}}{H}\left(|v'|-|u'|\right)\,\mathrm{d}\phi,$$

and combining with (B 1):

$$\begin{aligned} b\,(v(\phi_i)-u(\phi_i)) \leqslant & \int_0^{\phi_i}\frac{\chi_2}{|u'|}(v-u)'u'\,\mathrm{d}\phi + \int_0^{\phi_i}\frac{\tau_{2,y}}{H}\left(|v'|-|u'|\right)\,\mathrm{d}\phi \\ & + \int_{\phi_i}^{1}\frac{\chi_1}{|u'|}(v-u)'u'\,\mathrm{d}\phi + \int_{\phi_i}^{1}\frac{\tau_{1,y}}{H}\left(|v'|-|u'|\right)\,\mathrm{d}\phi. \end{aligned} \tag{B 3}$$

Now suppose that, for fixed Φ_i, the solution u_1 corresponds to $b = b_1$ and the solution u_2 corresponds to $b = b_2$. It is apparent that u_2 is a test solution for u_1 and vice versa. Inserting each into (B 3) and summing gives

$$\begin{aligned} (b_1-b_2)\,(u_2(\phi_i)-u_1(\phi_i)) \leqslant & \int_0^{\phi_i}\frac{\chi_2}{|u_1'|}(u_2-u_1)'u_1'\,\mathrm{d}\phi + \int_0^{\phi_i}\frac{\chi_2}{|u_2'|}(u_1-u_2)'u_2'\,\mathrm{d}\phi \\ & + \int_{\phi_i}^{1}\frac{\chi_1}{|u_1'|}(u_2-u_1)'u_1'\,\mathrm{d}\phi + \int_{\phi_i}^{1}\frac{\chi_1}{|u_2'|}(u_1-u_2)'u_2'\,\mathrm{d}\phi, \\ \leqslant & 0. \end{aligned} \tag{B 4}$$

The last statement follows from the general properties of convex functionals (see e.g. proposition 5.4 on page 25 of Ekeland & Témam 1976). In Pelipenko & Frigaard (2004*a*) it is shown that if χ_k is defined implicitly by equation (2.9) then the functional

$$F_k(x) = \int_0^{|x|^2}\frac{\chi_k(s^{1/2})}{2s^{1/2}}\mathrm{d}s \tag{B 5}$$

is Gateaux-differentiable and strictly convex, i.e. from this it follows that

$$\int_0^{\phi_i}\frac{\chi_2}{|u_1'|}(u_2-u_1)'u_1'\,\mathrm{d}\phi \leqslant \int_0^{\phi_i}F_2(u_2)-F_2(u_1)\,\mathrm{d}\phi,$$

and the various expressions on the right-hand side of (B 4) cancel out.

Therefore we have demonstrated that:

$$(b_2-b_1)\,(u_2(\phi_i)-u_1(\phi_i)) = (b_2-b_1)\,(q(\Phi_i,b_2)-q(\Phi_i,b_1)) \geqslant 0, \tag{B 6}$$

and $q\,(\Phi_i, b)$ is non-decreasing with respect to b. □

REFERENCES

Bittleston, S. H., Ferguson, J. & Frigaard, I. A. 2002 Mud removal and cement placement during primary cementing of an oil well; laminar non-Newtonian displacements in an eccentric Hele-Shaw cell. *J. Engng Maths* **43**, 229–253.

Ekeland, I. & Témam, R. 1976 *Convex Analysis and Variational Problems*. North-Holland.

Moyers-Gonzalez, M. A. & Frigaard, I. A. 2007*a* Kinematic instabilities in two-layer eccentric annular flows, part 1: Newtonian fluids. *J. Engng Maths* DOI 10.1007/*s*10665−007−9178−*y*.

Moyers-Gonzalez, M. A. & Frigaard, I. A. 2007*b* Kinematic instabilities in two-layer eccentric annular flows, part 2: shear-thinning and yield stress effects. *J. Engng Maths* (submitted).

Nelson, E. B. 1990 *Well Cementing*. Schlumberger Educational Services.

Payne, M. L., Wilton, B. S. & Ramos, G. G. 1995 Recent advances and emerging technologies for extended reach drilling. *Society of Petroleum Engineers Paper* SPE 29920.

Pelipenko, S. & Frigaard, I. A. 2004*a* On steady state displacements in primary cementing of an oil well. *J. Engng Maths* **48**, 1–26.

Pelipenko, S. & Frigaard, I. A. 2004*b* Two-dimensional computational simulation of eccentric annular cementing displacements. *IMA J. Appl. Maths* **64**, 557–583.

Pelipenko, S. & Frigaard, I. A. 2004*c* Visco-plastic fluid displacements in near-vertical narrow eccentric annuli: prediction of travelling wave solutions and interfacial instability. *J. Fluid Mech.* **520**, 343–377.

Sabins, F. L. 1990 Problems in cementing horizontal wells. *J. Petrol. Tech.* **42**, 398–400.

Zalesak, S. T. 1979 Fully multidimensional flux-corrected transport algorithms for fluids. *J.Comput. Phys.* **31**, 335.